

3D Radiation Hydrodynamic Simulations of Gravitational Instability in AGN Accretion Disks: Effects of Radiation Pressure

YI-XIAN CHEN (陈逸贤),¹ YAN-FEI JIANG (姜燕飞),² JEREMY GOODMAN,¹ AND EVE C. OSTRIKER¹

¹*Department of Astrophysical Sciences, Princeton University, Princeton, NJ 08544, USA*

²*Center for Computational Astrophysics, Flatiron Institute, New York, NY 10010, USA*

ABSTRACT

We perform 3D radiation hydrodynamic local shearing box simulations to study the outcome of gravitational instability (GI) in optically thick Active Galactic Nuclei (AGN) accretion disks. GI develops when the Toomre parameter $Q_T \lesssim 1$, and may lead to turbulent heating that balances radiative cooling. However, when radiative cooling is too efficient, the disk may undergo runaway gravitational fragmentation. In the fully gas-pressure-dominated case, we confirm the classical result that such a thermal balance holds when the Shakura-Sunyaev viscosity parameter (α) due to the gravitationally-driven turbulence is $\lesssim 0.2$, corresponding to dimensionless cooling times $\Omega t_{\text{cool}} \gtrsim 5$. As the fraction of support by radiation pressure increases, the disk becomes more prone to fragmentation, with a reduced (increased) critical value of α (Ωt_{cool}). The effect is already significant when the radiation pressure exceeds 10% of the gas pressure, while fully radiation-pressure-dominated disks fragment at $t_{\text{cool}} \lesssim 50\Omega^{-1}$. The latter translates to a maximum turbulence level $\alpha \lesssim 0.02$, comparable to that generated by Magnetorotational Instability (MRI). Our results suggest that gravitationally unstable ($Q_T \sim 1$) outer regions of AGN disks with significant radiation pressure (likely for high/near-Eddington accretion rates) should always fragment into stars, and perhaps black holes.

Keywords: AGN, accretion, star formation, gravitational instability, radiation pressure

1. INTRODUCTION

Supermassive black holes (SMBHs) have been found in the centers of most massive galaxies (see Kormendy & Ho 2013, for a review). They typically have masses ranging from $10^6 M_\odot - 10^9 M_\odot$, and harbor accretion disks which provide power to active galactic nuclei (AGN) and quasars (Lynden-Bell 1969).

The outer regions of such disks are thought to be heated at least partially by gravito-turbulence, a process extensively studied in contexts of protoplanetary disks (PPDs) as well as AGN accretion disks (e.g. Gammie 2001; Johnson & Gammie 2003; Rice et al. 2003, 2005). In a sufficiently extended standard thin accretion disk model (Shakura & Sunyaev 1973) with dimensionless viscosity parameter $\alpha < 1$ supporting a radially constant mass accretion rate (\dot{M})—perhaps due to Magnetorotational Instability (MRI) (Balbus & Hawley 1991)—there exists a self-gravitating radius r_{sg} beyond which the Toomre parameter Q_T (Toomre 1964)

drops below unity. Beyond this radius, which is typically around 0.01-0.1 pc for Eddington accretion rates and $M_{\text{SMBH}} \sim 10^8 M_\odot$, the disk becomes gravitationally unstable. Disks may however be able to self-regulate at $Q_T \gtrsim 1$, provided the mass-feeding rate is low enough that accretion and heating can be sustained with a gravitationally-produced α_{GI} not so large as to induce fragmentation. Analytical models have been applied to describe this region as a constant- Q_T disk in which the steady state turbulence from gravitational instability α_{GI} is an explicit function of distance to the SMBH, r , parameterized by the accretion rate \dot{M} and the value of Q_T (Goodman 2003; Goodman & Tan 2004; Sirko & Goodman 2003; Levin 2007).

In the case where both external heating and other sources of turbulence are weak, turbulence generated by gravitational instability must extract energy from the mean shear at a rate sufficient to offset radiative cooling, which requires $\alpha_{\text{GI}} \sim (\Omega t_{\text{cool}})^{-1} \equiv (\tau_{\text{cool}})^{-1}$ for local cooling time t_{cool} and orbital frequency Ω . Extensive simulations in the gas pressure dominated regime (e.g. Gammie 2001; Johnson & Gammie 2003; Rice et al. 2003) have led to the conclusion that if $\tau_{\text{cool}} \lesssim 3 - 5$, a

statistical steady state cannot be achieved, and the disk fragments. The exact value of the critical cooling time depends upon the equation of state (Rice et al. 2005), and still remains somewhat uncertain theoretically since numerical parameters such as resolution and integration time also appear to affect outcomes (Paardekooper 2012). The evolution and ultimate masses of the fragments is still under debate (Goodman & Tan 2004; Levin 2007).

As we move further out in radius in a constant- Q_T disk, radiative cooling becomes more efficient, and τ_{cool} continues to decrease until $\tau_{\text{cool}} \ll 1$ (especially when temperature drops to around 2000K and opacity becomes extremely small). Beyond this point disk fragmentation would seem to be inevitable, according to the simple $\tau_{\text{cool}} \lesssim 3$ criterion derived from gas-pressure-dominated simulations. Of course, in this situation, fragmentation is likely to lead to intense star formation, and the heat input from these stars may raise the sound speed and hence Q_T ; also, enhanced angular momentum transport via magnetized winds may further help to stabilize the disk by lowering the surface density required for a given accretion rate (Goodman 2003; Thompson et al. 2005).

In previous work, the influence of radiation pressure on the critical cooling timescale has rarely been studied, and uncertainty in the fragmentation condition prevents us from gaining a deeper understanding of how a gravito-turbulent, sub-parsec and optically thick region bridges the gap between the luminous inner accreting regions and the outer star-forming regions of an AGN disk. For moderate $\dot{M} \gtrsim 1M_{\odot}/\text{yr}$, radiation pressure dominates the total pressure within the gravitationally unstable disk region (Goodman 2003; Goodman & Tan 2004). A radiation-supported disk has a local effective adiabatic index of 4/3 and is much more prone to GI fragmentation than disk supported by completely ionized hydrogen pressure (analogous to some soft spots in the equation of state for partially dissociated hydrogen, which induce GI fragmentation in irradiated PPDs (Hirose & Shi 2017, 2019)). Indeed, simulations from Jiang & Goodman (2011) have shown that a high radiation-pressure fraction is able to push the critical τ_{cool} to values much larger than the order-unity critical value that holds in the gas-pressure-dominated regime. In other words, it is more difficult for a radiation-dominated disk to support quasi-steady turbulence whose dissipation balances cooling without runaway fragmentation.

The previous work of Jiang & Goodman (2011) employed shearing-sheet 2D simulations with a polytropic prescription for vertical hydrodynamical structure, and assumed an artificial prescription for radiative cooling

$\propto T^4$. While the results from these simulations were informative, this was primarily by way of identifying qualitative trends, given the highly simplified numerical treatment. In particular, since the cooling rate and the disk’s thermal response are key quantities that control GI, realistic thermodynamics and proper treatment of three-dimensional structure and radiation-gas interactions are essential to studying the non-linear evolution of GI in realistic AGN disks.

In this paper, we perform local shearing box simulations in 3D coupled with full radiation transport calculation, using the state-of-the-art implicit radiation module of Athena++ (Jiang 2021). Due to the high computational expense of radiative transfer calculations and the long thermal timescales in high optical depth environments, we focus on tracing the fragmentation boundary and only follow fragmenting cases up to the point of runaway collapse. We do not attempt to estimate the final masses of fragments, as this may involve prolonged processes of inflow and outflow, coalescence, and perhaps nuclear burning, and would probably require subgrid models to avoid extreme demands on numerical resolution. We follow quasi-steady cases for a few hundred dynamical timescales.

This paper is organized as follows: In §2, we lay out the theoretical framework for some basic scalings of thermodynamic quantities in the local parameter space assuming quasi-steady state, as well as their connection to a $Q_T \sim 1$ global disk model. In §3 we introduce our numerical setup for radiation hydrodynamic (RHD) simulations, including initial conditions, boundary conditions, diagnostics, and methods of determining fragmentation. Our results are presented and summarized in §4. Our models include both cases that result in quasi-steady turbulence and those that undergo fragmentation, and both gas pressure and radiation pressure dominated regimes. We discuss the implication of our results and future prospects in §5.

2. THEORETICAL FORMULATION AND BASIC SCALINGS

As an idealized local model of an accretion disk, one of the main advantages of the shearing box is that it is defined by a small number of control parameters that should remain constant as the system evolves. For simulations of gravito-turbulence, the principle control parameters of a Keplerian (i.e. shearing factor $q \equiv -d \ln \Omega / d \ln r = 3/2$) shearing box are the surface density of mass, Σ , and the rotation rate, Ω . In combination with Newton’s constant G , we can construct dynamically relevant units of time, length, and mass:

$$t_* \equiv \Omega^{-1}, \quad l_* \equiv \frac{\pi G \Sigma}{\Omega^2} \equiv \pi^{-1} L_T, \quad m_* \equiv \Sigma l_*^2. \quad (1)$$

The length l_* represents the pressure scale height when Toomre's stability indicator $Q_T \equiv \Omega c_s / (\pi G \Sigma)$ is unity, and characteristic sound speed $c_s \rightarrow l_*/t_*$. Another important lengthscale is the ‘‘Toomre length’’ L_T , which carries an additional factor of π , corresponding to the 2D Jeans length $c_s^2/(G\Sigma)$, or half the wavelength of the marginally unstable mode, at $Q_T \sim 1$. Note that c_s (defined in terms of the *total* pressure) is not included among the control parameters: instead, c_s needs to be regarded as an *output* parameter of our models, determined by the balance between turbulent heating and radiative cooling, though again we expect the steady-state c_s to correspond to $Q_T \sim 1$.

To a state determined by (Σ, Ω) and $Q_T \sim 1$ one must add physical parameters to describe the equation of state and cooling of the gas. In scale-free 2D (Gammie 2001) or 3D (Shi & Chiang 2014) local simulations, there were only two such parameters: an adiabatic index γ relating the gas internal energy per unit mass to its 2D or 3D gas pressure $U_{\text{gas}} = P_{\text{gas}}/(\gamma - 1)$, and a Newtonian characteristic cooling timescale t_{cool} , or equivalently, the dimensionless product $\tau_{\text{cool}} = \Omega t_{\text{cool}}$. Our case is somewhat more complex because we model the radiation field by which the matter cools, such that instantaneous cooling rates are determined by physical values of Ω, Σ and the variable Q_T (or equivalently c_s), and we are particularly interested in regimes where the radiation also contributes significantly to the pressure support of matter.

2.1. Relative Contribution from Radiation and Gas Pressure

Before addressing cooling, we discuss the equation of state and temperature profiles, having in mind conditions near the midplane where optical depths are large and the gas and radiation temperatures are equal. From the dynamical units (Equation 1), one can form a combination with units of pressure: $P_* = m_* l_*^{-1} t_*^{-2} = \pi G \Sigma^2$, as well as units of density $\rho_* = m_* l_*^{-3} = \Omega^2 / \pi G$.

At $Q_T \sim 1$, we can generally express the midplane or some characteristic total pressure and density as $P = f_p P_*$ and $\rho = f_\rho \rho_*$, where $f_p, f_\rho = \mathcal{O}(1)$ are dimensionless constants depending on the detailed vertical structure and Q_T , while T is the midplane or some characteristic temperature.

The total pressure is the sum of the gas and radiation pressure:

$$\frac{\rho k_B T}{\mu} + \frac{a T^4}{3} = P_{\text{gas}} + P_{\text{rad}} = P,$$

$$\text{or } \frac{f_\rho \Omega^2}{\mu \pi G} (k_B T) + \frac{\pi^2}{45} \frac{(k_B T)^4}{(\hbar c)^3} = f_p \pi G \Sigma^2. \quad (2)$$

Here, μ is the molecular weight of gas. This is directly analogous to the Eddington quartic for the central conditions in non-degenerate stars (e.g. Goodman & Tan 2004). As in that case, Equation 2 can be regarded as a quartic equation for the temperature. There is a single positive root to the quartic, whereby T becomes a function of (Σ, Ω) .

It is convenient to introduce a symbol for the ratio of pressures:

$$\Pi \equiv \frac{P_{\text{rad}}}{P_{\text{gas}}} = \frac{a T^3 \mu}{3 \rho k_B}. \quad (3)$$

This is equivalent to $(1 - \beta)/\beta$ in the stellar-structure literature (e.g., Goodman & Tan 2004). At $\Pi = 1$, the two terms on the left side of Equation 2 are equal, such that (T, Ω, Σ, μ) are related at $\Pi = 1$ by

$$k_B T = \left(\frac{45 f_\rho \Omega^2}{\pi^3 G \mu} \right)^{1/3} \hbar c, \quad \text{and}$$

$$f_p^3 f_\rho^{-4} = \frac{360}{\pi^2} \frac{(\hbar c)^3}{(\pi G)^7} \frac{\Omega^8}{\mu^4 \Sigma^6}, \quad (4)$$

$$\approx 6.4 \Omega_{-8}^8 \Sigma_5^{-6} \mu_{0.6}^{-4},$$

with $\Omega_{-8} = \Omega / (10^{-8} \text{ rad s}^{-1})$, $\Sigma_5 = \Sigma / (10^5 \text{ g cm}^{-2})$, and $\mu_{0.6} = \mu / (0.6 m_p)$, for proton mass m_p .

More generally, Equation 2 can be rewritten in terms of the pressure ratio as

$$\Pi^{1/3} + \Pi^{4/3} = \left[f_p^3 f_\rho^{-4} \frac{\pi^2}{45} \frac{(\pi G)^7}{(\hbar c)^3} \mu^4 \Sigma^6 \Omega^{-8} \right]^{1/3} \quad (5)$$

$$\approx [1.3 f_p^3 f_\rho^{-4} \mu_{0.6}^4 \Sigma_5^6 \Omega_{-8}^{-8}]^{1/3},$$

the solution of which gives the function $\Pi(\Sigma, \Omega)$. Here it is evident that $\Pi = \text{Const.}$ solutions have $\Sigma \propto \Omega^{4/3}$. Furthermore, requiring that vertical hydrostatic equilibrium is satisfied constrains f_p and f_ρ as functions of Q_T only.

As a quantitative example, Figure 1 shows contours of the pressure ratio Π and the midplane temperature T_0 (subscript ‘‘0’’ specifically denotes midplane) as functions of (Σ, Ω) , for a specific self-similar vertical disk profile that assumes an altitude-independent Π and a mass-weighted $Q_T = 1$ (see Section 3.2 for details; Q_T is defined formally in Equation 22). This family of solutions of Equation 2 and Equation 5 holds specifically for $f_p(Q_T = 1) = 0.66$ and $f_\rho(Q_T = 1) = 0.74$.

Neglecting all constants including f_p and f_ρ , it is easy to see that

$$\begin{aligned} T &\propto \Sigma^2 \Omega^{-2}, & \Pi &\propto \Sigma^6 \Omega^{-8} & \text{if } \Pi \ll 1 \\ T &\propto \Sigma^{1/2}, & \Pi &\propto \Sigma^{3/2} \Omega^{-2} & \text{if } \Pi \gg 1. \end{aligned} \quad (6)$$

One can understand the situation more easily by comparing these scalings with the change in slope of the

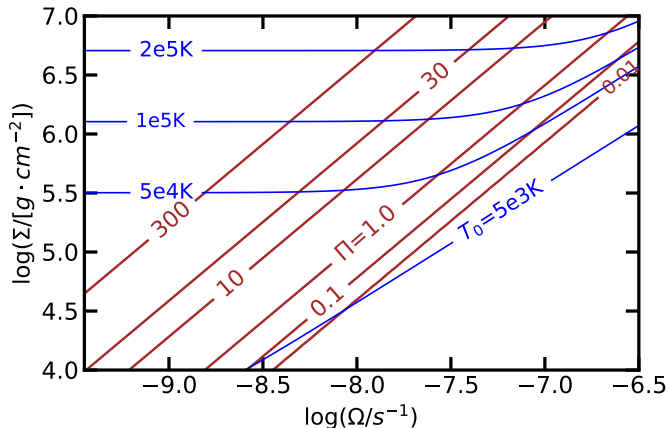


Figure 1. Contours of pressure ratio Π (brown red) and the midplane temperature T_0 (blue) in the Σ, Ω plane, assuming a vertically constant Π and $Q_T = 1$ initial condition as described in §3.2. Q_T is defined formally in Equation 22.

contours in Figure 1 across $\Pi = 1.0$. From the gas to radiation pressure dominated regime, the contours of Π become sparser and the T_0 contours flatten out after crossing $\Pi = 1.0$.

To summarize, instead of considering only the gas pressure and internal energy in the equation of state, the total internal energy is given by the sum of gas and radiation internal energy $U = P_{\text{gas}}/(\gamma-1) + 3P_{\text{rad}}$, with their relative contribution determined by Π as a function of (Σ, Ω) , which itself follows different scalings in the limits $\Pi \gg 1$ and $\Pi \ll 1$. In the remainder of this paper, we take $\gamma = 5/3$ as for a fully ionized plasma.

2.2. Cooling Timescales

Although not explicitly involved in the pressure ratio Π , the opacity (κ) should be important for the *strength* of the turbulence, because the heating rate and cooling rate must balance on average in a gravito-turbulent state, with the latter being sensitive to κ through the vertical optical depth of the system τ . Nevertheless, with κ generally being a function of (ρ, T) , the cooling rate is also expressible in terms of the combination (Σ, Ω) with the constraint $Q_T \sim 1$. Specifically, for constant opacity applicable to high temperature, we have $\tau \equiv \kappa \Sigma / 2$, and the radiative energy flux from each of the two disk surfaces can be approximated as (Johnson & Gammie 2003)

$$F_{z,\text{max}} = \sigma T_{\text{eff}}^4 = \frac{8\sigma T_0^4}{3\tau} = \frac{16\sigma T_0^4}{3\kappa\Sigma}. \quad (7)$$

One can then calculate the realistic cooling timescale

$$t_{\text{cool}} = U_{2D} / 2F_{z,\text{max}}, \quad (8)$$

which is the inverse of cooling rate. Here $U_{2D} = \int_z U dz = f_U P_* l_*$ is the vertically integrated internal energy per unit area, while f_U is yet another order-unity coefficient determined by the vertical profile, slightly more complicated than f_ρ, f_p in the sense that it has a small dependency on the pressure weighting Π that manifests mainly in the $\Pi \sim 1$ transition region. The dimensionless $\tau_{\text{cool}} = \Omega t_{\text{cool}}$ is the cooling time measured in units $t_* = \Omega^{-1}$.

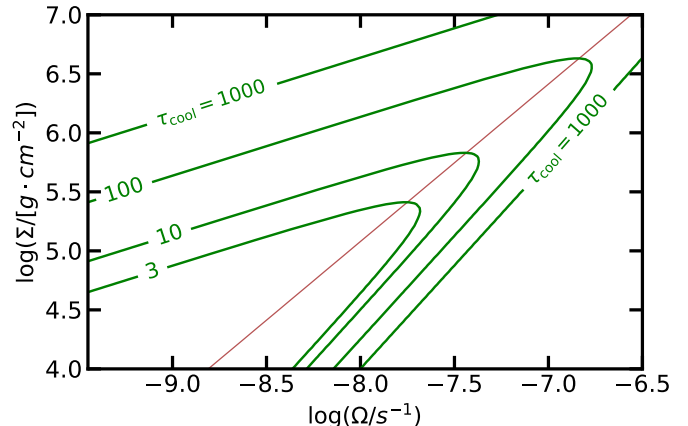


Figure 2. Contours of τ_{cool} in the Σ, Ω plane, assuming a vertically constant Π and $Q_T = 1$ initial condition as described in §3.2. The brown line is the $\Pi = 1$ contour.

Similar to Figure 1, we plot contours of τ_{cool} for our specific example of vertical distribution in Figure 2, which follow from numerical results of $T(\Sigma, \Omega)$ (Figure 1) and the specific choice for $f_U(Q_T = 1) = 1 - 1/(2 + 2\Pi)$ corresponding to our self-similar vertical profile. The trends here can also be understood in a simple manner by checking proportionality scalings in two different regimes combining Equation 6 and Equation 8. When κ is constant, $F_z \propto T^4 \Sigma^{-1}$, applying $U_{2D} \sim P_* l_*$ we have

$$\begin{aligned} \tau_{\text{cool}} &\propto \Sigma^{-4} \Omega^7 & \text{if } \Pi \ll 1 \\ \tau_{\text{cool}} &\propto \Sigma^2 \Omega^{-1} & \text{if } \Pi \gg 1. \end{aligned} \quad (9)$$

The scalings in Equation 9 imply that as we start from the lower-right gas pressure dominated regime, for increasing Σ or decreasing Ω , τ_{cool} always reaches a minima (maxima for cooling rate) around $\Pi \approx 1$ before increasing again in the radiation dominated regime.

Specially, we can write down a more explicit expression for the cooling timescale in the $\Pi \gg 1$ regime, where $aT_0^4 = 3P_0 = 3f_p P_*$:

$$\begin{aligned} \tau_{\text{cool}} &\approx \frac{f_U P_* l_* \Omega \times 3\kappa \Sigma}{8caT_0^4} = \frac{f_U c_s}{8f_p c} \times \kappa \Sigma \\ &= \frac{\pi f_U \kappa G \Sigma^2}{8f_p c \Omega}, \quad \Pi \gg 1 \end{aligned} \quad (10)$$

In §4.5 we will see this is closely related to a radiative diffusion criterion.

It has been shown by extensive simulations that in the classical gas pressure dominated regime, the fragmentation boundary is roughly determined by an approximate value of $\tau_{\text{cool}} \sim 3$ (Gammie 2001; Johnson & Gammie 2003; Rice et al. 2003; Shi & Chiang 2014). Another way to interpret this conclusion is that in thermal equilibrium, turbulent heating must balance cooling such that $\alpha \sim \tau_{\text{cool}}^{-1}$, and the critical α a steady state gas disk could allow cannot exceed ~ 0.3 . Such a boundary would suggest that the lower-left region of the parameter space within $\tau_{\text{cool}} < 3$ represent transient states that will fragment and cannot be maintained by gravito-turbulence, unless other heating sources are involved.

Following Jiang & Goodman (2011), we expect the disk to be more subject to fragmentation when radiation pressure dominates. Specifically, the maximum α that a quasi-steady state could support decreases with the growth of Π . As a result, the fragmentation regime can no longer be constrained by some universal value of τ_{cool} , but should span to larger τ_{cool} for increasing Π , possibly covering any value of τ_{cool} when $\Pi \gg 1$.

Realistic opacities can have complicated dependencies at low temperature, which should modify the cooling rate contours in the gas-dominated regime (e.g. Johnson & Gammie 2003, Figure 7), especially when temperature drops to around 2000K and opacity becomes extremely small (Thompson et al. 2005). In this paper, however, we adopt a constant opacity in order to isolate the effects of the pressure ratio Π .

2.3. Accretion Rates in Steady-state

To link local simulations with global structure of AGN disks, we introduce the scaling for a kind of “expected” local accretion rate \dot{M} . Under assumption that in steady-state where heating provided by gravito-turbulence balances radiative cooling rates given by τ_{cool} , every point on the (Σ, Ω) plane also corresponds to a local accretion rate (Pringle 1981; Jiang & Goodman 2011):

$$\dot{M} = \frac{8\pi F_{z,\text{max}}}{3\Omega^2} \propto F_{z,\text{max}} \Omega^{-2}, \quad (11)$$

The proportionality can also be derived from

$$\dot{M} \propto \alpha c_s^2 \Sigma \Omega^{-1}, \alpha \sim \tau_{\text{cool}}^{-1}, \quad (12)$$

at a $Q_T = 1$ steady-state (Gammie 2001). For our specific vertical profile, we plot in Figure 3 exact contours of \dot{M} calculated from Equation 11 in our numerical profiles. Combining Equation 7 and Equation 11, in two

limits \dot{M} conforms with the scalings

$$\begin{aligned} \dot{M} &\propto \Sigma^7 \Omega^{-10} & \text{if } \Pi \ll 1 \\ \dot{M} &\propto \Sigma \Omega^{-2} & \text{if } \Pi \gg 1. \end{aligned} \quad (13)$$

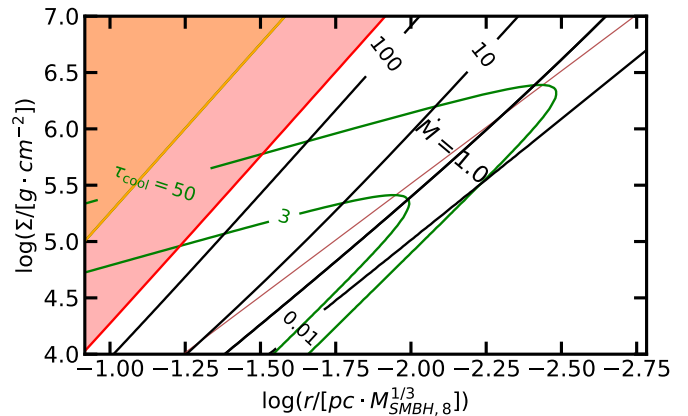


Figure 3. Contours of \dot{M} (black, in $M_{\odot} \text{yr}^{-1}$) and τ_{cool} (green), assuming the initial condition as described in §3.2, and turbulent heating that balances the cooling rate given in Figure 2. The brown line is the $\Pi = 1$ contour. The abscissa is re-written in terms of radius r scaled by the SMBH mass, where $M_{\text{SMBH},8} = M_{\text{SMBH}}/10^8 M_{\odot}$. We also map out highly super-Eddington regions where \dot{M} exceeds 100 times the Eddington value for $M_{\text{SMBH}} = 10^8$ (pink region) and $10^9 M_{\odot}$ (orange region), for radiative efficiency $\eta = 0.1$ and Eddington luminosity.

As we follow contours of constant \dot{M} in Figure 3, we see how τ_{cool} and Π varies radially along a disk with given accretion rate. Because \dot{M} contours are always steeper than Π contours, a $Q_T \sim 1$ accretion disk always becomes radiation dominated at sufficiently small r . For example, the $\dot{M} = 1 M_{\odot}/\text{yr}$ contour (roughly half the Eddington rate for $M_{\text{SMBH}} = 10^8 M_{\odot}$) intersects $\Pi = 1$ a bit below $\tau_{\text{cool}} \sim 50$. In fact, as r increases, both Π and τ_{cool} decrease along each \dot{M} contour, albeit with the latter being much more sensitive. Beyond some large radius, τ_{cool} falls below a critical value which is either ~ 3 for $\Pi \ll 1$ or possibly larger for $\Pi > 1$, and we inevitably enter a star-forming region of fragmentation, which may also provide self-regulated heating to maintain $Q_T \sim 1$ (Thompson et al. 2005). Since star formation would therefore be able to strip away large fractions of \dot{M} before reaching the inner disk, this suggests it would be difficult for a super-Eddington constant- \dot{M} flow to penetrate into inner gravito-turbulent parts of the disk. We map out regions where \dot{M} exceeds 100 Eddington value for $M_{\text{SMBH}} = 10^8$ (pink region) and $10^9 M_{\odot}$ (orange region), assuming accretion efficiency $\eta = L/\dot{M}c^2 = 0.1$ and the luminosity L equals the Eddington luminosity. Such accretion rates may be achieved temporarily if

mass were dumped into the disk by violent events such as mergers or Tidal Disruption Events (TDEs), or if the formed massive stars themselves can lose mass that feeds the central SMBH (Cantiello et al. 2021).

Apart from the outer boundary of the gravito-turbulent region constrained by some lower limit of τ_{cool} , in realistic situations we also need to consider an inner boundary of the $Q_T = 1$ disk region given by the upper limit $\tau_{\text{cool}} \lesssim 50$. For larger τ_{cool} , the heating rate of MRI turbulence, which typically gives $\alpha_{\text{MRI}} \sim 0.02$ (Beckwith et al. 2011; Simon et al. 2012), is already adequate to heat the disk up to $Q_T > 1$ and shut off gravitational instability, and we enter the inner standard thin disk region (Shakura & Sunyaev 1973). In other words, even if a $Q_T \sim 1$ disk heated solely by gravito-turbulence were stable at sufficiently long $\tau_{\text{cool}} \gg 3$ in the far upper left region of Figure 3, solutions in that part of parameter space would not be physical due to extra heating from MRI that would realistically be present.

It follows from the above discussion that in the (Σ, Ω) parameter space, a classical model for a $Q_T \sim 1$, sub-Eddington gas pressure dominated disk can be simply parameterized as a low- \dot{M} contour constrained within $\tau_{\text{cool}} \in [3, 50]$, representing a gravito-turbulent region sandwiched between an inner gravitationally stable standard thin disk powered by MRI, and an outer star-forming region (Goodman (2003); Thompson et al. (2005)). While the above describes behavior at low accretion rates, uncertainty in the fragmentation limit for higher $\dot{M} \gtrsim M_\odot/\text{yr}$ disks in the $\Pi \gtrsim 1$ regime prevents us to assert the same conclusion for the radiation dominated regime. In this paper, we will apply hydrodynamic simulations with full radiative transfer to check the validity of the classical fragmentation condition in the gas pressure dominated regime, and to explore how the fragmentation condition is modified at increasing values of Π .

3. METHODS

3.1. Equations Solved

We adopt the 3D shearing box configuration in Athena++ (Stone et al. 2020), and solve ideal hydrodynamic equations coupled with the time-dependent, frequency-integrated radiation transport equation for specific intensities over discrete angles (Jiang et al. 2014; Jiang 2021; Goldberg et al. 2021):

$$\frac{\partial \rho}{\partial t} + \nabla \cdot (\rho \mathbf{v}) = 0 \quad (14)$$

$$\begin{aligned} \frac{\partial(\rho \mathbf{v})}{\partial t} + \nabla \cdot (\rho \mathbf{v} \mathbf{v} + \mathbf{P}_{\text{gas}}) &= -\rho \nabla \Phi \\ -2\rho \Omega \hat{\mathbf{z}} \times \mathbf{v} + 2q\rho \Omega^2 x \hat{\mathbf{x}} - \rho \Omega^2 z \hat{\mathbf{z}} - \mathbf{G}_r \end{aligned} \quad (15)$$

$$\begin{aligned} \frac{\partial E}{\partial t} + \nabla \cdot (E + P_{\text{gas}}) \mathbf{v} &= -\rho \mathbf{v} \cdot \nabla \Phi \\ &+ \rho \Omega^2 \mathbf{v} \cdot (2qx \hat{\mathbf{x}} - z \hat{\mathbf{z}}) - cG_r^0 \end{aligned} \quad (16)$$

$$\frac{\partial I}{\partial t} + c\mathbf{n} \cdot \nabla I = S(I, \mathbf{n}) \quad (17)$$

In these equations, ρ is the gas density, \mathbf{v} is the 3D flow velocity and $q = 3/2$ is the Keplerian shear parameter. \mathbf{P}_{gas} and P_{gas} are the gas pressure in tensorial and scalar form, respectively: i.e., $\mathbf{P}_{\text{gas}} = P_{\text{gas}} \mathbf{1}$ if $\mathbf{1}$ represents the unit tensor. The gas mean molecular weight $\mu = 0.6m_p$ is that of a fully ionized gas at solar abundance. $E = U_{\text{gas}} + \rho v^2/2$ is the sum of gas internal energy $U_{\text{gas}} = P_{\text{gas}}/(\gamma-1)$ and the kinetic energy $\rho v^2/2$ where $\gamma = 5/3$. The vertical component of the external gravity by the central star is added as source terms in the equation for momentum and energy transport. The source terms \mathbf{G}_r and G_r^0 are the time-like and space-like components of the radiation four-force (Mihalas & Mihalas 1984). I is the frequency-integrated intensity and \mathbf{n} is the photon propagation direction unit vector.

The hydrodynamic equations are solved using the standard Godunov method in Athena++ (Stone et al. 2020). We use the second-order Van-Leer method for the time integration, and the HLLC Riemann solver to calculate the flux for hydrodynamic quantities. We adopt second-order reconstruction for intensity as well as hydrodynamic quantities. The disk self-gravitational potential is obtained by solving the Poisson equation

$$\nabla^2 \Phi = 4\pi G \rho, \quad (18)$$

using fast Fourier transforms (Koyama & Ostriker 2009; Kim et al. 2011). For each radiative transfer calculation, we update the intensity in the co-moving frame $I_0(\mathbf{n}_0)$ (which is Lorentz-transformed from the lab frame $I(\mathbf{n})$) by the source term S_0 in the comoving frame:

$$S_0(I_0, \mathbf{n}_0) = c\rho\kappa_P \left(\frac{caT^4}{4\pi} - J_0 \right) + c\rho(\kappa_s + \kappa_R)(J_0 - I_0) \quad (19)$$

then convert it back to the lab frame. Here κ_s is the electron scattering opacity, κ_R is the Rossland mean opacity, and κ_P is the Planck opacity. In this work, we adopt a constant electron scattering opacity $\kappa_s = 0.4\text{cm}^2/\text{g}$ and a fiducial $\kappa_R = 0.05\text{cm}^2/\text{g}$ that is non-zero but subdominant. We also choose $\kappa_P = 0.05\text{cm}^2/\text{g}$ under the gray opacity approximation. While realistic Planck opacities may be larger (Jiang & Blaes 2020), this value suffices as long as the radiation field is adjusted to be in temperature equilibrium with gas, which turns out to be the case in our simulations. See Jiang (2021) for more details on implementation of radiation.

3.2. Initial Conditions

The initial equilibrium profile of our self-gravitating disk is assumed to be horizontally homogeneous, while the vertical distribution is derived semi-analytically. The initial surface density Σ and orbital frequency Ω are needed as input parameters. For convenience, we define a midplane gravitational instability factor that is a proxy for Toomre Q_T :

$$Q = \frac{\Omega^2}{2\pi G \rho_0}, \quad (20)$$

where ρ_0 is the density in the midplane (subscript denotes midplane quantities). Following the method of Jiang & Goodman (2011), with a given Q we derive density and pressure distribution $\rho(z)$ and $P(z)$ for a self-gravitating constant- Π polytrope within the photosphere, combined with an isothermal radiation field outside the photosphere; see Appendix A for details. We confirm that initial hydrostatic equilibrium holds before the disk starts to cool.

From the expressions for midplane ρ_0 and pressure P_0 , we find (see Equation A6) the coefficients $f_\rho(Q)$ and $f_p(Q)$ for our specific version of the midplane EoS quartic (Equation 2 & Equation 5) that determines the solution of Π , T_0 . The problem remaining is to choose appropriate values of Q and to connect with the classical Toomre value Q_T , technically defined in a razor-thin 2D disk (e.g. Johnson & Gammie 2003). The sound speed, written explicitly as

$$c_s = \left(\frac{P_{\text{gas}} + P_{\text{rad}}}{\rho} \right)^{1/2} \quad (21)$$

is well defined in an isothermal 3D disk as a constant, with $Q_T = \sqrt{2/\pi} Q$.

When c_s is not a constant, as in our polytropic vertical profile, it is still possible to define some Q_T which reflects vertically-averaged properties, such as

$$Q_T = \frac{[c_s^2]_\rho^{1/2} \Omega}{\pi G \Sigma} \quad (22)$$

where $[c_s^2]_\rho$ is a density-weighted average of the square sound speed, directly connected to the vertically integrated pressure:

$$[c_s^2]_\rho \equiv \frac{\int_z c_s^2 \rho dz}{\int_z \rho dz} = \frac{\int_z (P_{\text{gas}} + P_{\text{rad}}) dz}{\Sigma} \quad (23)$$

This Q_T , defined similarly to Equation 9 of Booth & Clarke (2019) or Equation 13 of Riols et al. (2017), has the advantage of capturing the vertically averaged properties and will smoothly connect to the global average

quantity Q_T in §3.5. Combined with Equation A7 expressing $P_{2D} = \int_z P dz$ in terms of Q, Σ, Ω , we see that the midplane Q and the average Q_T are linked through

$$Q_T = \sqrt{\frac{Q I_4(Q)}{16 [I_3(Q)]^3}}, \quad (24)$$

Through approximations given in Equation A3, we understand that $Q_T \propto Q$ when they are large but $Q_T \propto \sqrt{Q}$ when $Q \ll 1$ (the strongly self-gravitating limit).

Referring to Equation A8, the coefficient f_U can be more simply expressed as:

$$f_U = Q_T^2 \left[1 - \frac{1}{2(\Pi + 1)} \right] \quad (25)$$

With a “reference plane” parameterized by $Q_T = 1$, corresponding to $Q = 0.76$, we solve quartic equations for Π and T_0 as functions of Σ, Ω as shown in Figure 1, making use of $\rho_0 = f_\rho \rho_* = 0.74 \rho_*$ and $P_0 = f_p P_* = 0.66 P_*$. Combining the vertically integrated internal energy density per area U_{2D} with the vertical radiative flux beyond the photosphere $F_{z,\text{max}}$, we can calculate $\tau_{\text{cool}}(\Sigma, \Omega)$ (Equation 8) as shown in Figure 2. Lastly, we can link the local parameter space with global accretion rates using $\dot{M}(\Sigma, \Omega)$ (Equation 11) as shown in Figure 3. One can refer back to §2 for general scalings of these contours in the $\Pi \gg 1$ and $\Pi \ll 1$ limits¹.

Practically, in our simulations, by default we start from a $Q_T \approx 1.05, Q \approx 0.82$ state slightly hotter than in the reference plane, such that we allow gravitational instability to gradually develop during an initial passive cooling phase. As a result, contours in Figure 1, Figure 2 are not exactly the initial Π and τ_{cool} of our profiles, but rather the “expected” values of some time-average value for τ_{cool} and Π if turbulent heating can support a steady state at $Q_T \approx 1$ with a similar vertical structure as the initial condition.

As we shall see, our vertical structure is a useful approximation for the final gravito-turbulent quasi-steady states within the photosphere, at least for gas pressure dominated cases, but usually on average $Q_T \gtrsim 1.1$ in the final states, which results in a generally hotter state with larger time-averaged Π' than the “expected” values. In fragmentation cases, there are no steady-state values to be measured so the reference contours are not self-consistent with the outcome, but if additional heat

¹ The scalings are valid for any polytropic vertical density profile. Numerically, the initial total vertically integrated U_{2D} does not follow the analytical expectation $f_U P_* l_*$ exactly due to the existence of an isothermal radiation field outside the photosphere, but the deviation is very small.

source is considered the disk may still settle into a steady state (Thompson et al. 2005).

We adopt code units such that Ω , Σ , and the Toomre length $L_T \equiv \pi^2 G \Sigma / \Omega^2$ are unity; our length and mass units are therefore larger than the quantities l_* and m_* defined in Equation 1 by factors of π and π^2 , respectively. Expressed in such units, we have a universal initial profile for ρ, T parametrized only by Q regardless of Σ, Ω (e.g. Figure 9). The code unit for energy density is therefore $\Sigma \Omega^2 L_T = \pi^2 G \Sigma^2$, and that of temperature is $(L_T \Omega)^2$.

We initialize a decaying turbulence field using the default setup of **Athena++**, which distributes an assigned total turbulence kinetic energy E_{turb} across wavenumber $m_{\min} = 1$ to $m_{\max} = 16$ with a spectral slope that we choose to be -2. We choose $E_{turb}/U \sim \tau_{\text{cool}}^{-1}$ such that E_{turb} may smoothly connect to an instability-generated turbulence that balances cooling. In a long-term steady state, the outcome should not depend on details of the initial turbulence field. We also tested some representative fragmentation cases with different m_{\max} and confirmed convergence.

3.3. Box Sizes and Resolution

The default box size for our simulations is $L_x \times L_y \times L_z = 8 \times 8 \times 2(L_T^3)$. Due to the computational expense of full three-dimensional RHD, the default low resolution with which we run long-term simulations for quasi-steady or marginally stable cases is $N_x \times N_y \times N_z = 128 \times 128 \times 32$. In certain cases with high optical depth, we also found it necessary to simulate with a larger box size to prevent strong outflow, such that $L_z = 4$ and $N_z = 64$. For most of our short-term fragmenting cases, we can afford to test with a doubled resolution $N_x \times N_y \times N_z = 256 \times 256 \times 64$ keeping the default box size. In certain radiation dominated cases, where it is necessary to resolve the Jeans length defined by gas pressure rather than total pressure, we also performed extra tests with smaller box sizes and higher resolution; see §4.5 for details. Table 1 lists the full set of input parameters for all runs discussed in the paper.

3.4. Boundary Conditions

For radiation and hydrodynamic variables we apply the standard shearing-periodic boundary condition in x and periodic boundary condition in y . We implement an open outflow boundary condition in z by setting the density, pressure and radiation intensity in the boundary cells to the same values as the last active cells. Additionally, we copied both the velocity and the radiative flux from the final cell to the ghost zones in the z direction, but reset the velocity and radiative flux in the z

direction to zero if flows are directed into the simulation box to prevent artificial mass and energy injection. The Poisson solver for Φ applies shearing-periodic boundary condition in x periodic boundary condition in y , and vacuum boundary conditions in z . We implement floor values such that T does not fall below 10^{-3} of the initial midplane temperature T_0 , and ρ does not fall below 10^{-6} of the initial midplane density ρ_0 . Because our floor values are sufficiently small, in most of our simulations we were able to prevent significant mass loss and achieve mass conservation without the need of artificial mass-rescaling, e.g. applied in Booth & Clarke (2019).

3.5. Diagnostics

To facilitate analysis of our simulation results, we first introduce notation for some scalar history variables obtained by averaging physical quantities over space and time. We define the volume average $\langle X \rangle$ as:

$$\langle X \rangle \equiv \frac{\int X dx dy dz}{\int dx dy dz}. \quad (26)$$

With this definition, instantaneous values of the dimensionless stress parameters that characterize angular momentum transport are defined as

$$\alpha_R = \frac{\langle R_{xy} \rangle}{\langle P_{rad} + P_{gas} \rangle}, \quad \alpha_g = \frac{\langle G_{xy} \rangle}{\langle P_{rad} + P_{gas} \rangle} \quad (27)$$

$$R_{xy} = \rho v_x \delta v_y, \quad G_{xy} = g_x g_y / 4\pi G$$

where $\delta v_y = v_y + q\Omega x$, the perturbed y velocity subtracting out the background shear flow. We have verified that contribution of the stress term from radiation viscosity (e.g. ?, Equation 15) is negligible in our simulations, in contrast to the situation in low optical depth disk surface regions within coronae caused by magnetic dissipation and vertical temperature inversion (?).

We define the density-weighted mean square sound speed

$$\langle c_s^2 \rangle_\rho \equiv \frac{\int_z c_s^2 \rho dx dy dz}{\int_z \rho dx dy dz}, \quad (28)$$

and the midplane average of density

$$\langle \rho \rangle_{\text{mid}} \equiv \frac{\int \rho(z=0) dx dy}{\int dx dy}, \quad (29)$$

such that the ‘‘Toomre-like’’ history variables

$$Q_T = \frac{\langle c_s^2 \rangle_\rho^{1/2} \Omega}{\pi G \langle \Sigma \rangle}, \quad Q = \frac{\Omega^2}{2\pi G \langle \rho \rangle_{\text{mid}}}, \quad (30)$$

start exactly from initial values of Q_T, Q at $t = 0$ as defined in the §3.2.

In the analysis of vertical profiles, we calculate the horizontally-averaged vertical distribution of quantity X as a function of z via:

$$\langle X(z) \rangle \equiv \frac{\int X(x, y, z) dx dy}{\int dx dy}. \quad (31)$$

To normalize the vertical coordinate, we define a fiducial scale height as

$$h = \frac{\langle \Sigma \rangle}{2\langle \rho \rangle_{\text{mid}}}. \quad (32)$$

To achieve good convergence in the averaging of radiation to gas pressure ratio, we find that it is preferable to define

$$\Pi' \equiv \frac{\int P_{\text{rad}} dx dy dz}{\int P_{\text{gas}} dx dy dz}, \quad \Pi'(z) \equiv \frac{\int P_{\text{rad}}(x, y, z) dx dy}{\int P_{\text{gas}}(x, y, z) dx dy}, \quad (33)$$

instead of directly averaging Π .

The dimensionless cooling time is defined as

$$\tau_{\text{cool}} = \frac{\int U dx dy dz}{\int \sum |F_z|(z = \pm z_{\text{max}}) dx dy} \Omega \quad (34)$$

where U is the internal energy density of gas and radiation, and $\int |F_z|(z = \pm z_{\text{max}}) dx dy$ is the total energy cooling rate by radiative flux directed outwards from the two vertical boundaries.

Time averages of our history variable are denoted as

$$\langle X \rangle_t \equiv \frac{\int X dt}{\int dt} \quad (35)$$

where the integration is over the time after saturation, as indicated in Table 2.

We also define the running time average of history variables starting from t_i as

$$\langle X \rangle_{t' < t}(t) \equiv \frac{\int_{t_i}^t X dt'}{\int_{t_i}^t dt'}; \quad (36)$$

this is helpful in visualizing convergence of strongly fluctuating variables such as stress parameters.

3.6. Determining bound objects

To confirm fragmentation, we verify formation of gravitationally bound objects using the method of Mao et al. (2020), which is an extension of the GRID-core algorithm (Gong & Ostriker 2011). In short, for each local minimum in the gravitational potential field Φ , we first identify the closed contour with the largest value of $\Phi = \Phi_{\text{max}}$ which contains no other local minima. Within this region of interest (referred to as an HBP for “hierarchical binding parent”), we narrow the region down to cells where

$$\int E_{\text{turb}} + U + \rho(\Phi - \Phi_{\text{max}}) < 0, \quad (37)$$

is satisfied when integrated up to some contour $\Phi' \leq \Phi_{\text{max}}$, meaning gas is bound relative to the potential contour Φ_{max} . Here E_{turb} is the turbulent kinetic energy relative to the center of mass of the region, which is referred to as an HBR (for “hierarchical bound region”). With this definition, material within the HBR, as a whole, does not have enough turbulent kinetic and thermal energy to move into a neighboring potential minimum. If the gravitational well of an HBP is deep enough, the entire HBP becomes an HBR.

4. RESULTS

4.1. General Categorization

We summarize initial parameters for all our runs in Table 1, and categorize outcomes into turbulent, fragmentation, and marginal cases. In addition to the control parameters Σ, Ω , and the initial τ_{cool}, Π (defined at initial $Q_T \approx 1.05$, see §3.2), we also record the total length of simulations t_{final} in terms of Ω^{-1} .

In the short-term fragmentation cases, compact density waves start to form within the first $\sim \tau_{\text{cool}}$ and eventually break into bound clumps. Just a few Ω^{-1} after the initial formation of bound clumps, their central regions become extremely dense, and in this situation of spatially unresolved gravitational collapse the Riemann solver fails. We practically terminate the simulation around this time and declare a runaway fragmentation.

In other cases, growth of overdensity is limited by shear and structures are dispersed before they grow too compact. In this situation, we only see transient clump formation in either a) the initial adjustment stage for the gravito-turbulent cases, or b) throughout the entire simulation for the marginal cases.

In cases where there is not immediate gravitational runaway, the disk usually settles into a quasi steady-state thermal equilibrium after the development of turbulence, which happens around a few cooling times. However, it can be difficult to determine a clean boundary between gravito-turbulence and fragmentation due to the existence of certain marginal cases. In these cases, bound clumps never exist for longer than a few orbital times, but because of large stochastic excursions the disk cannot maintain the steady excitation and dissipation of turbulence needed in order for heating to balance cooling. The features of these scenarios will be described in detail below, but here we remark that without runaway collapse, both gravito-turbulent and marginal cases can both be run for much longer timescales, at least for a number of τ_{cool} . Nevertheless, all quasi-steady time-average values in §3.5 are only well-defined in the quasi-steady turbulence states.

Model	$\Sigma(\text{g}/\text{cm}^2)$	$\Omega(\text{s}^{-1})$	$\tau_{\text{cool}}(t=0)$	$\Pi(t=0)$	Box Size (L_T^3)	Resolution	$t_{\text{final}}\Omega$	Outcome
S2e4O7e-9	2.0×10^4	7.0×10^{-9}	3.95	0.0042	$8 \times 8 \times 2$	$128 \times 128 \times 32$	100	Turbulence, Figure 9
fiducial	5.0×10^4	1.2×10^{-8}	4.56	0.013	–	–	150	–, Figure 5 - 9, 16
fiducial_res	–	–	–	–	–	$256 \times 256 \times 64$	100	–, Figure 7,9
S1e5O2.2e-8	1.0×10^5	2.2×10^{-8}	19.32	0.0068	–	$128 \times 128 \times 32$	150	–, Figure 9
S2e5O3.6e-8	2.0×10^5	3.6×10^{-8}	38.19	0.0084	–	–	250	–, Figure 9
S5e5O6.3e-8	5.0×10^5	6.3×10^{-8}	52.16	0.022	–	–	250	–, Figure 9
S2e6O1.2e-7	2.0×10^6	1.2×10^{-7}	48.01	0.27	–	–	100	Severe outflow
S2e6O1.2e-7_z	–	–	–	–	$8 \times 8 \times 4$	$128 \times 128 \times 64$	400	Turbulence, Figure 9
S2e6O2e-8_res	–	2×10^{-8}	112.81	30.24	$4 \times 4 \times 2$	$256 \times 256 \times 128$	300	–, Figure 15 - 19
S2e4O6e-9*	2.0×10^4	6.0×10^{-9}	1.40	0.014	$8 \times 8 \times 2$	$256 \times 256 \times 64$	20	Fragmentation
S2e4O2.5e-9	–	2.5×10^{-9}	0.11	1.30	–	–	3	–
S5e4O1e-8*	5.0×10^4	1.0×10^{-8}	1.49	0.051	–	–	15	–
S5e4O8e-9	–	8.0×10^{-9}	0.56	0.20	–	–	10	–
S5e4O5e-9	–	5.0×10^{-9}	0.33	1.28	–	–	4	–
S1e5O1.8e-8*	1.0×10^5	1.8×10^{-8}	5.26	0.031	–	–	30	–, Figure 11, 12
S1e5O1.5e-8	–	1.5×10^{-8}	2.01	0.11	–	–	18	–, Figure 11, 12
S1e5O1e-8	–	1×10^{-8}	0.81	0.73	–	–	15	–
S1e5O2e-9	–	1.5×10^{-8}	2.82	34.15	–	–	6	–, Figure 13 ,14, 19
S2e5O2.8e-8*	2.0×10^5	2.8×10^{-8}	7.99	0.055	–	–	30	–
S2e5O1.5e-8	–	1.5×10^{-8}	1.86	1.07	–	–	10	–
S3e5O4e-9	3.0×10^5	4×10^{-9}	12.72	44.58	–	–	25	–, Figure 13 ,14, 19
S5e5O5.5e-8*	5.0×10^5	5.5×10^{-8}	23.54	0.060	–	–	40	–
S5e5O5e-8	–	5.0×10^{-8}	14.82	0.11	–	–	25	–
S5e5O3e-8	–	3.0×10^{-8}	5.85	1.05	–	–	10	–
S2e6O1e-7	2.0×10^6	1.0×10^{-7}	35.62	0.60	–	–	40	–
S1e5O2e-9_res	1.0×10^5	2×10^{-9}	2.82	34.15	$4 \times 4 \times 2$	$256 \times 256 \times 128$	8	–
S3e5O4e-9_res	–	–	–	–	–	–	30	–
S1e5O2e-8	1.0×10^5	2.0×10^{-8}	10.23	0.014	$8 \times 8 \times 2$	$128 \times 128 \times 32$	200	Marginal
S2e5O3.4e-8	2.0×10^5	3.4×10^{-8}	26.12	0.013	–	–	200	–
S5e5O6e-8	5.0×10^5	6.0×10^{-8}	38.63	0.032	–	–	300	–

Table 1. Summary of simulation input parameters. – means “as above.” Cases with * have corresponding runs with $2\times$ coarser resolution which demonstrate very similar properties; we omit them in this table.

In the (Σ, Ω) plane, the outcome of our runs can be qualitatively summarized in Figure 4, where each symbol represents ≥ 1 simulation. Extra care should be taken for some points that are run with different resolution in the radiation-dominated regime, as elaborated in §4.5. Generally, we observe that while fragmentation cases (red) and gravito-turbulent cases (blue) separated along the $\tau_{\text{cool}} \sim 3 - 5$ contour in the gas-pressure dominated limit to the lower right ($\Pi \lesssim 0.1$), the fragmentation boundary shifts to larger τ_{cool} as one increases the radiation pressure fraction towards $\Pi = 1.0$, with some marginal cases (purple) in between. This indicates that it is more difficult to maintain gravito-turbulence against strong cooling in more radiation dominated disks. As we shall show below, this trend is more quanti-

tatively defined by comparing the time averaged $\langle \tau_{\text{cool}} \rangle_t$ and $\langle \Pi' \rangle_t$ in the final states of gravito-turbulent cases.

4.2. The Fiducial Gravito-Turbulent Run

We start by investigating classical gravito-turbulent states in the $\Pi \ll 1$ limit. Such steady states are expected to self-regulate at $\langle \tau_{\text{cool}} \rangle_t > 3$ and $Q_T \gtrsim 1$ (e.g. Johnson & Gammie 2003; Rice et al. 2003). To find a fiducial case in the classical gas pressure dominated limit, we start along the $\tau_{\text{cool}} = 3$ contour at $\Sigma = 5 \times 10^4 \text{g}/\text{cm}^2$ on our parameter map (Figure 4). Finding that $\Omega = 10^{-8} \text{s}^{-1}$ leads to fragmentation, we shift towards slightly larger $\Omega = 1.2 \times 10^{-8}$, with longer τ_{cool} . This model, as indicated by the blue square in Figure 4, evolves to reach a quasi-steady gravito-turbulent state. In principle, we could start from the far right where $\tau_{\text{cool}} \gg 1$ and then probe leftwards for a fragmen-

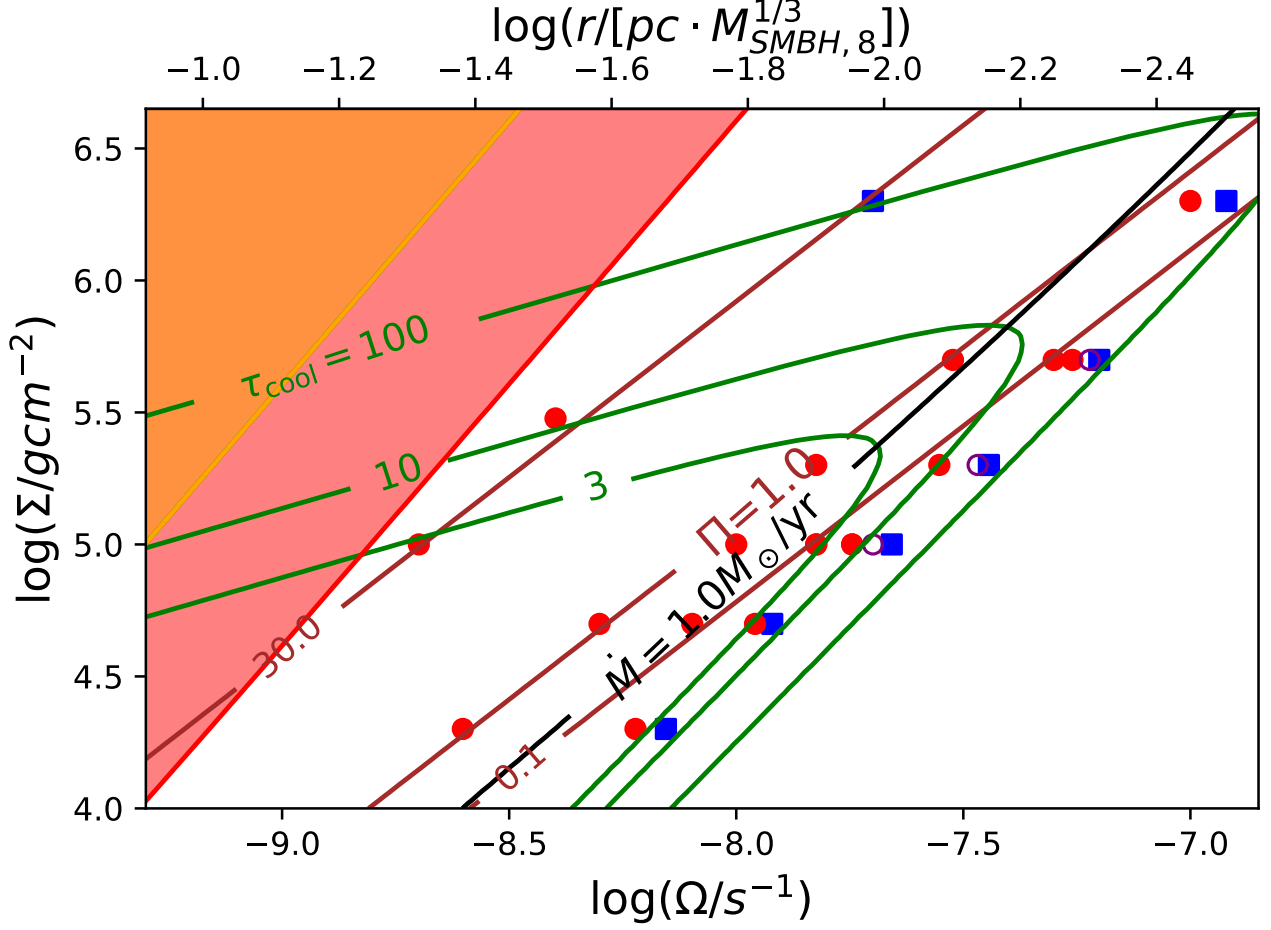


Figure 4. Similar to Figure 1, Figure 2, Figure 3, but each extra point represents outcome of simulations run with a set of Σ, Ω parameters. Red dots and blue squares represent fragmentation and gravito-turbulent cases, respectively, while purple circles represented marginal cases. The definition of other contours and shaded regions are the same as in Figure 3.

tation boundary, but it would be expensive to run many gravito-turbulence simulations for a few times τ_{cool} . Instead, our strategy is to start from cases with the lowest $\langle \tau_{\text{cool}} \rangle_t \sim \tau_{\text{cool}}$ possible along each constant Σ (or optical depth). This makes it possible to run simulations for timescales much longer than the local cooling time.

We present results of the fiducial case at $\Sigma = 5 \times 10^4 \text{g/cm}^2$, $\Omega = 1.2 \times 10^{-8} \text{s}^{-1}$ in Figures 5, 6, 7, 8. Snapshots of the midplane ρ, T and Π distribution at the end of the simulation $t = 150\Omega^{-1}$ are shown in Figure 5, when gravito-turbulence has long since reached a quasi-steady state. Evolution of globally averaged variables $\alpha, Q_T, \Pi', \tau_{\text{cool}}$ (definitions see §3.5) collected at a cadence of $0.1\Omega^{-1}$ are shown in Figure 6, from which we see that the disk undergoes a small initial cooling phase as Q_T dips below 1 before growth of stress parameters.

The disk reaches a quasi-steady state after $t \sim 25\Omega^{-1}$, and we run the simulation up to $t = 150\Omega^{-1}$. This gives us 20-30 average cooling timescales $\langle \tau_{\text{cool}} \rangle_t$ dur-

ing our averaging interval $t_{\text{ave}} = 125\Omega^{-1}$, from 25-150 Ω^{-1} , which is more than sufficient for running averages of fluctuating quantities to converge. For example, although it is easy to see that other global quantities have reached quasi-steady oscillation from Figure 6, the stress parameter α and its components are fluctuating on a sub-orbital frequency with large amplitude. In Figure 7 we show in solid lines the running averages of the stress parameters starting from $25\Omega^{-1}$ for the fiducial case (solid lines), which converge to steady values after a few tens of dynamical timescales. The heating produced when the total stress is $\langle \alpha \rangle_t \sim 0.17$ is able to balance the average cooling timescale of $\langle \tau_{\text{cool}} \rangle_t \sim 5.62$, which is slightly longer than the initial value $\tau_{\text{cool}} = 4.56$. The final $\langle \Pi' \rangle$ reaches 0.034, which is ~ 3 times larger than the initial value 0.013, suggesting a slightly hotter final state than the fiducial initial condition.

We also run the fiducial parameter model at higher resolution and confirm that the averaged history out-

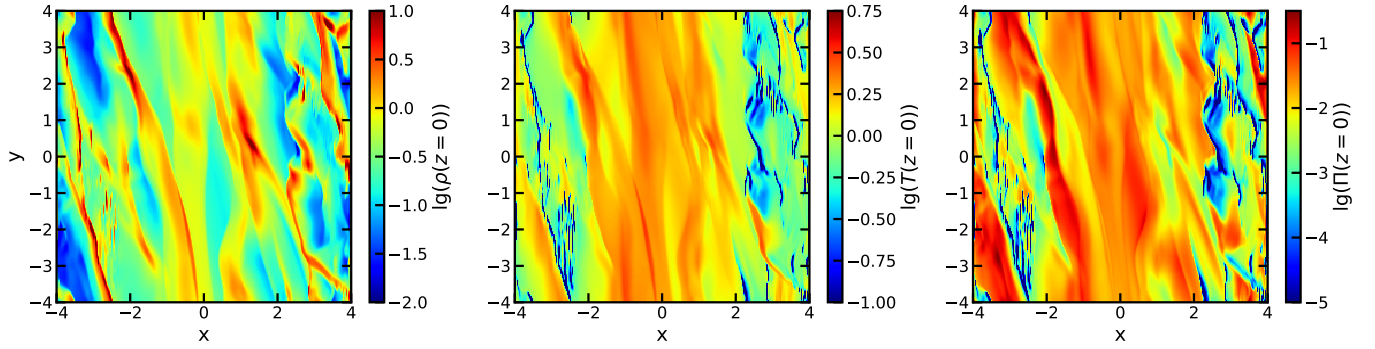


Figure 5. Slices of midplane density, temperature, and radiation pressure fraction Π in the fiducial simulation at the final time ($t = 150\Omega^{-1}$). The density and temperature are normalized by initial midplane values for a $Q_T \sim 1.05$ disk. The length unit is $L_T = \pi^2 G \Sigma / \Omega^2$.

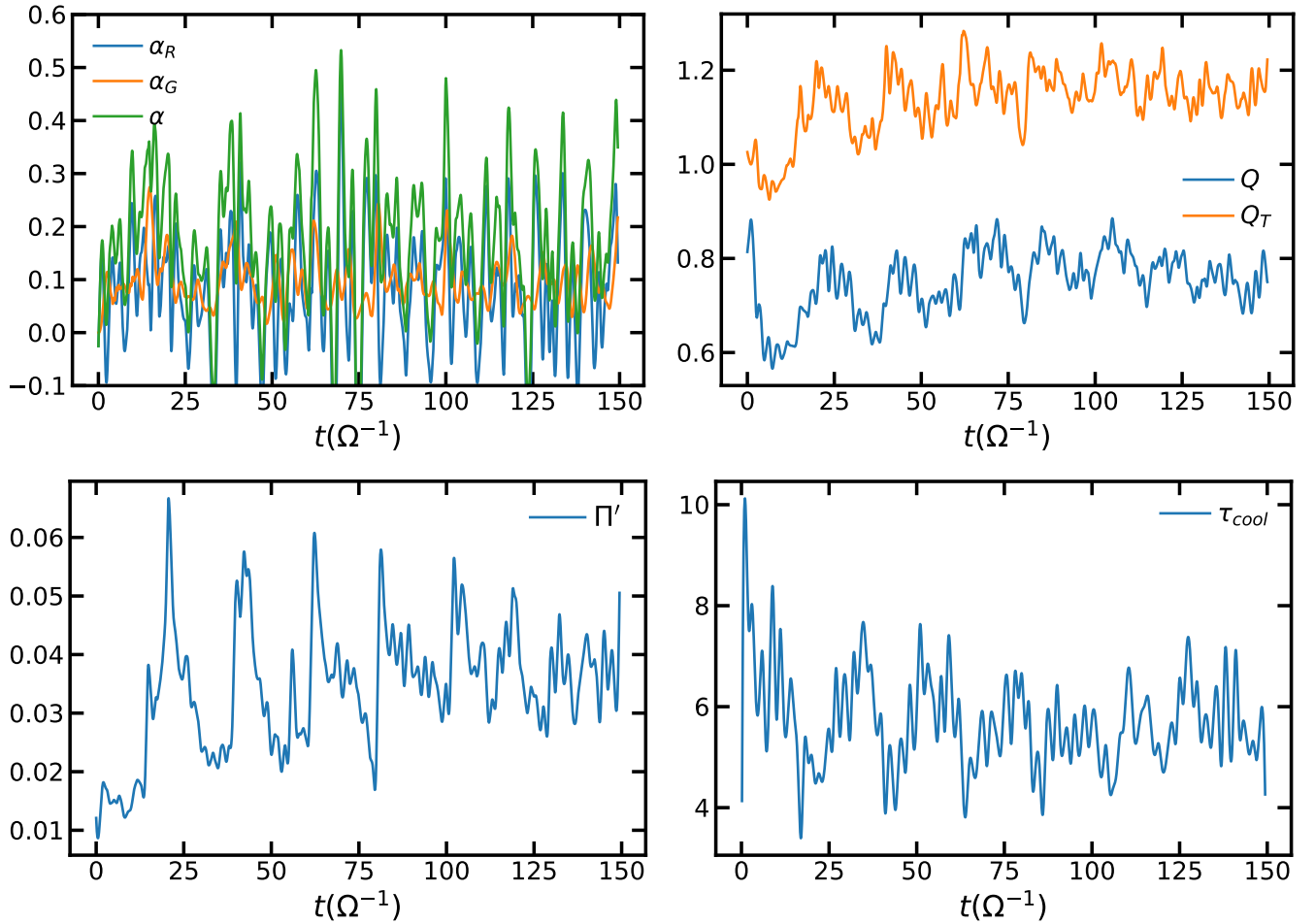


Figure 6. The evolution of globally averaged variables α , Q_T , Π' , and τ_{cool} in our fiducial simulation. These average variables are defined in §3.5.

puts and average vertical profile converge with the standard resolution run. The running averages of stress parameters from the high resolution run `fiducial_res` are shown in Figure 7 as dashed lines (averaging starts at $30\Omega^{-1}$ when disk enters a steady state), which converge to values similar to the standard run after $100\Omega^{-1}$. All other averaged vital variables are collected in Table 2 under the entry `fiducial` and `fiducial_res`. The average $\langle\tau_{\text{cool}}\rangle_t$ after $100\Omega^{-1}$ is slightly longer for the high-resolution run than the standard run, and the radiation fraction is slightly smaller. The computational cost for this high resolution run is about 3 Million CPU core hours. Given this high expense, for subsequent long-term simulations for gravito-turbulence states, we mainly adopt the standard resolution.

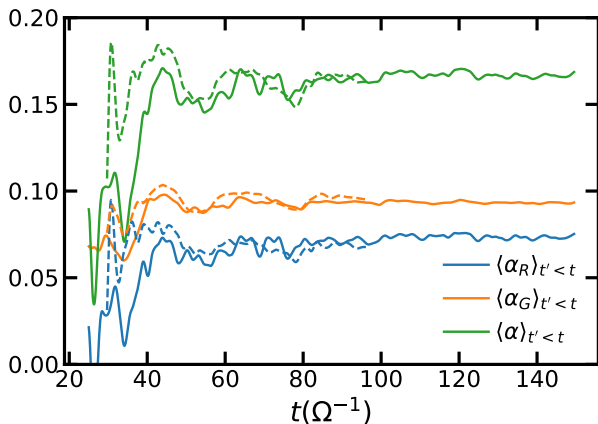


Figure 7. Running time-average of stress parameters in the fiducial gravito-turbulent model (solid lines) and the doubled resolution run of the same model (dashed lines).

The time-averaged vertical distribution $\rho(z)$, radiation, gas temperature $T_{\text{rad}}(z), T_{\text{gas}}(z)$ and total gas pressure P_{gas} in our fiducial run are plotted in Figure 8. The initial ρ , $T_{\text{gas}} = T_{\text{rad}}$, and P_{gas} vertical profiles are plotted in dotted lines. In steady-state, the gas and radiation are in thermal equilibrium, but the temperature and density profiles are generally more extended than the initial polytrope within the photosphere. The temperature and density gradient relaxes from our initial configuration and becomes much less steep around the photosphere. The temperature (radiation energy density) outside the photosphere region is isothermal, although it has little effect on the general gravito-turbulence since gas is tenuous in that optically-thin region. The average vertical $\langle\Pi'(z)\rangle_t$ distribution within the photosphere is close to constant in our fiducial case (see Figure 9), not too far from our initial assumption. However, but we shall see this may not be valid for larger Π' runs when we compare a sequence of

vertical profiles for gravito-turbulence cases in Figure 9, normalized by the midplane values of the averaged profiles themselves.

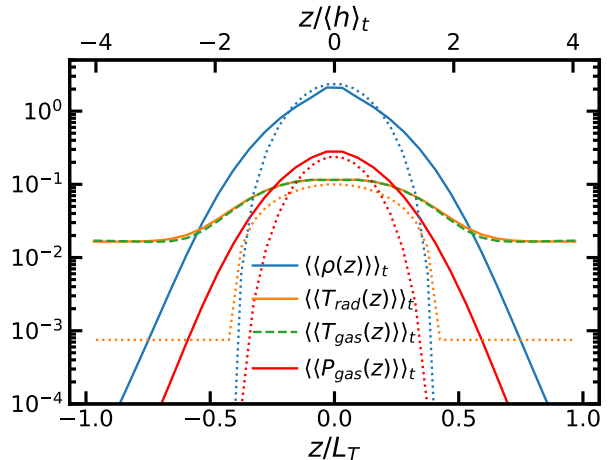


Figure 8. Solid lines: the horizontally and temporally averaged vertical distribution of density, gas/radiation temperature, and gas pressure in code units for our fiducial run, after quasi-steady state is reached. Dotted lines show the initial vertical profiles of the run, corresponding to constant Π . The top axis is normalized in terms of the averaged scale height.

4.3. Gas Pressure Dominated Gravito-Turbulent States

Starting from our fiducial case which lies to the right of the stability boundary, we continue to explore the Σ, Ω plane as indicated with points shown in Figure 4. In the $\Pi \ll 1$ limit, we identify another steady case at a smaller surface density $\Sigma = 2 \times 10^4 \text{g/cm}^2$. The initial midplane temperature is 2000K so constant opacity is not in practice realistic, but this case does have $\langle\tau_{\text{cool}}\rangle_t = 4.11$, which serves the purpose of validating consistency with the $\tau_{\text{cool}} \gtrsim 3$ classical fragmentation criterion.

Exploring along the other direction of expected τ_{cool} contours with increasing Π , we further identify 4 four gravito-turbulent cases, plotted as blue squares in Figure 4. The parameters for all these runs are summarized in the first part of Table 1, and outcomes for averages of variables are summarized in Table 2. We perform time averages starting from $t = t_{\text{final}} - t_{\text{avg}}$ to the end of the simulation t_{final} , where t_{avg} is listed in Table 2.

In Figure 9 we show the averaged vertical distributions of density, temperature, vertical radiation flux as well as pressure ratios of these cases, with the vertical axis normalized in terms of average scale height $\langle h \rangle_t$. Density and temperature profiles $\bar{\rho}, \bar{T}$ are normalized by the midplane value, and \bar{F}_z is normalized by $|F_{z, \text{max}}|$

model	$t_{\text{avg}}\Omega$	$\langle Q_T \rangle_t$	$\langle Q \rangle_t$	$\langle \alpha \rangle_t$	$\langle \alpha_G \rangle_t$	$\langle \alpha_R \rangle_t$	$\langle \tau_{\text{cool}} \rangle_t$	$\langle \Pi' \rangle_t$	$\langle h \rangle_t$	$\langle \tau_{\text{cool}} \rangle_t / \tau_{\text{cool}}(t=0)$	$\langle \Pi' \rangle_t / \Pi(t=0)$
S2e4O7e-9	80	1.08	0.70	0.18	0.10	0.081	4.11	0.022	0.22	1.04	5.24
fiducial	125	1.15	0.76	0.17	0.093	0.075	5.62	0.034	0.24	1.23	2.62
fiducial_hi	70	1.11	0.73	0.16	0.095	0.069	6.48	0.029	0.23	1.42	2.23
S1e5O2.2e-8	80	1.22	0.79	0.17	0.087	0.086	6.44	0.035	0.25	0.33	5.15
S2e5O3.6e-8	150	1.25	0.80	0.10	0.047	0.053	12.08	0.048	0.25	0.32	5.71
S5e5O6.3e-8	150	1.36	0.87	0.048	0.025	0.033	20.52	0.12	0.27	0.39	5.45
S2e6O1.2e-7_z	150	1.42	0.94	0.023	0.012	0.011	42.17	1.04	0.30	0.88	3.85
S2e6O2e-8_res	300	1.19	0.84	0.0062	0.0018	0.0044	150.63	38.31	0.23	1.34	1.27

Table 2. Summary of outcomes in gravito-turbulent cases. Initial conditions are given in the upper portion of Table 1.

at the disk surface. Darker curves represent cases with larger time-averaged Π' , and in this case, also larger optical depth $\kappa\Sigma/2$. The fiducial high resolution case is plotted with dashed lines. All the solid lines represent cases run with standard resolution.

Most cases adopt a standard box size, with the exception of S2e6O1.2e-7_z which applied $8L_T \times 8L_T \times 4L_T$ with doubled grid number in the vertical axis (ergo same resolution). The standard box size cases all have $\langle \Pi' \rangle_t < 1$, and the vertical distribution of quantities share similar profiles plotted in terms of the scale height. Within $\pm 2\langle h \rangle_t$, these profiles are similar to the initial polytrope, with $\langle \Pi' \rangle_t$ undergoing little change within one scale height, although the normalization $\langle h \rangle_t$ (measured in units $L_T = \pi l_*$) itself is an increasing function of Σ , consistent with an increasing $\langle Q_T \rangle_t$ in quasi-steady state. The radiation pressure becomes dominant outside the photosphere, where temperature and gas density are low and cannot affect disk dynamics.

Run S2e6O1.2e-7_z with radiation comparable to gas pressure stands out because its profile becomes much more extended than the initial condition, and we have to apply a larger box to accommodate the quasi-steady profile. In fact, the box size was adjusted after we found in run S2e6O1.2e-7 that the standard box size leads to severe mass outflow. This is why in Figure 9 for all other cases only $L_T \langle h \rangle_t^{-1} \lesssim 5$ scale heights are covered on either side but for S2e6O1.2e-7_z we cover $2L_T \langle h \rangle_t^{-1} \sim 7$ scale heights on each side. Compared with other runs at smaller $\langle \Pi' \rangle_t$, the vertical temperature profile does not drop as rapidly as a function of z in S2e6O1.2e-7_z. Towards the boundaries, the density profile is less steep, and since temperature also drops off more slowly, $\Pi'(z)$ has a large deviation from the midplane value.

The stress parameters' vertical profiles are plotted in the bottom panels of Figure 9. For this purpose, they are normalized by $\alpha \langle (P_{\text{gas}} + P_{\text{rad}}) \rangle_t(z=0)$ (as indicated by the overline) such that $\int \langle \langle R_{xy}(z) \rangle \rangle_t + \langle \langle G_{xy}(z) \rangle \rangle_t dz = 1$. We see that the extended temperature profile of S2e6O1.2e-7_z is consistent with having velocity fluctu-

ations which give rise to non-negligible Reynolds stress outside the photosphere, while in other cases both gravitational and Reynolds stress are appreciable only near the midplane.

Before discussing outcomes of fragmentation, we can already gain some understanding of the effect of Π' from these quasi-steady states along the stability boundary. We plot the time-averaged $\langle \alpha \rangle_t$ as functions of $\langle \tau_{\text{cool}} \rangle_t$ and $\langle \Pi' \rangle_t$ in Figure 10. The upper panel demonstrates energy balance since $\alpha \approx \tau_{\text{cool}}^{-1}$. Furthermore, we expect these variables to roughly trace out the shortest cooling timescale the disk could maintain stability against, or the largest turbulence strength the disk could possibly support.

From the lower panel of Figure 10, we see that for $\Pi' \ll 1$ we recover the classical boundary where α has a limit of $\lesssim 0.2$, while $\tau_{\text{cool}} \gtrsim 5$. As we increase Π' at higher Σ , we expect the effect of radiation pressure to extend the instability threshold to larger cooling time and smaller turbulence. Previous results from Jiang & Goodman (2011) suggest that when $\Pi' > 1$ the maximum quasi-steady stress α a disk could generate starts to deviate from ~ 0.3 , decreasing down to $\lesssim 0.01$ at $\Pi' \gtrsim 30$. In our simulations, we observe that $\Pi' \sim 0.1$ is already sufficient to modify the stability boundary significantly such that the disk can only support $\alpha \lesssim 0.05$ with $\tau_{\text{cool}} \gtrsim 20$. When Π' reaches order unity, the gravitationally-driven stress has dropped to $\alpha \sim 0.02$, comparable to the level that can be provided by MRI (Beckwith et al. 2011; Simon et al. 2012). Although in this preliminary study, we have too few simulation data points to produce a robust empirical prescription for this dependence, simply extrapolating from the current trend towards $\langle \Pi' \rangle_t$ of order 10, we expect a maximum gravitationally-driven turbulent stress $\alpha < 0.01$ for the highly radiation dominated regime. As discussed in Section 2, such a configuration may not be realistic since MRI can already provide sufficient heating to turn off GI and the problem reduces to a thin α disk model. Further implications are discussed in §5.

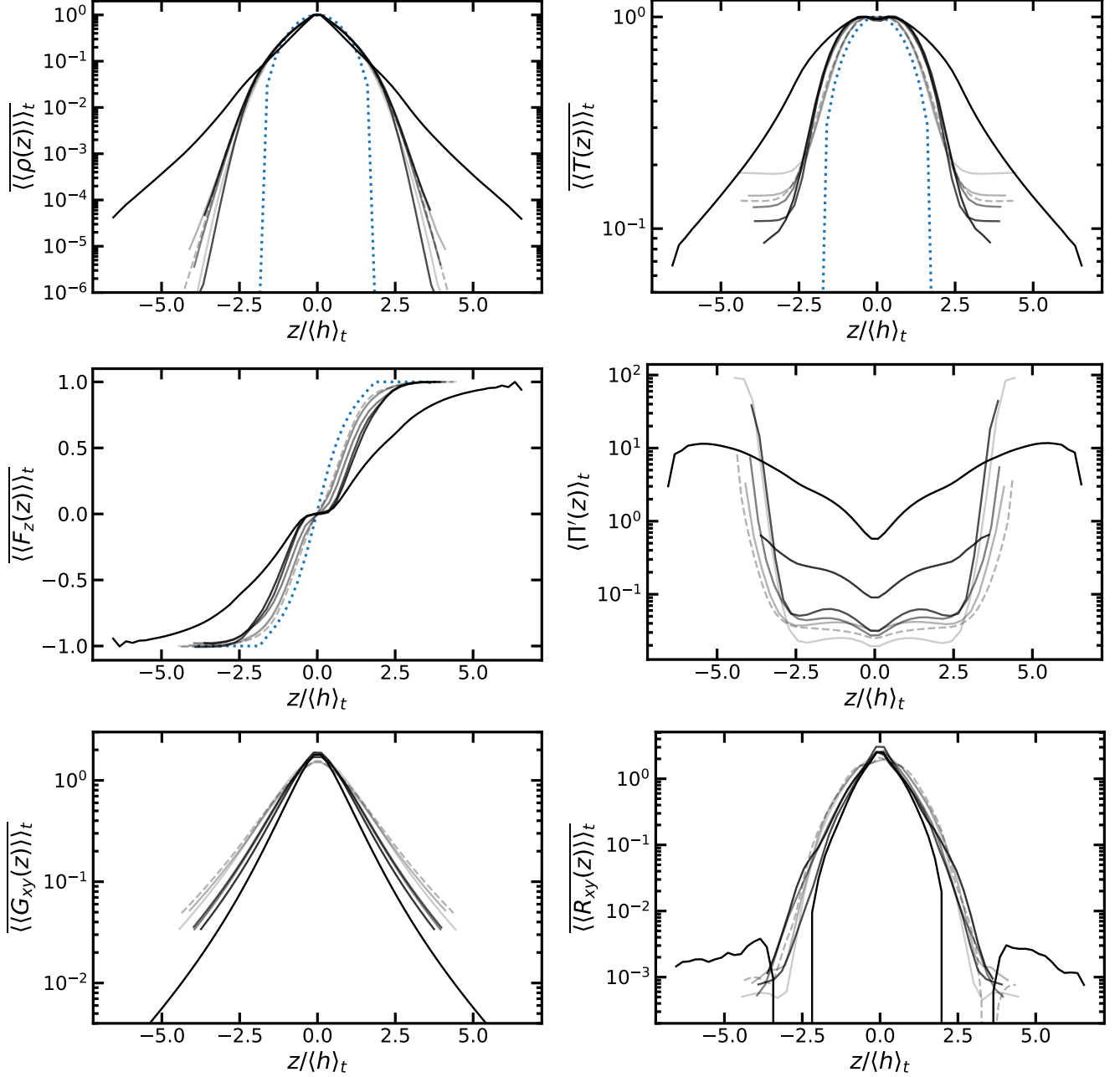


Figure 9. Horizontally and temporally averaged vertical distributions of density, temperature, vertical radiative flux, pressure ratios, and stress functions in the quasi-steady gravito-turbulent cases. Darker curves represent cases with larger Σ and radiation pressure fraction. Dotted lines show the adopted initial vertical distribution. All profiles are normalized (as indicated by overline); see text.

4.4. Gas Pressure Dominated Fragmentation Cases

Simulation cases that lead to fragmentation are plotted as red dots in Figure 4. After roughly an initial τ_{cool} , radiative cooling leads to development of bound objects. We plot in Figure 11 the midplane density and Π distribution for exemplary fragmentation cases S1e501.5e-8 and S1e501.8e-8 after the formation of bound objects. The brown contours indicate boundaries for HBPs, while

dashed black contours indicate bound regions (see §3.6). The overlapping of these contours means entire HBPs are bound, satisfying the HBR condition.

The evolution of spatially averaged variables $\Pi', Q, \tau_{\text{cool}}$ for these cases are plotted in Figure 12. both the initial Π and the final average Π' at the point of fragmentation is ~ 0.1 ; therefore the overall conditions are of gas pressure-dominated fragmentation.

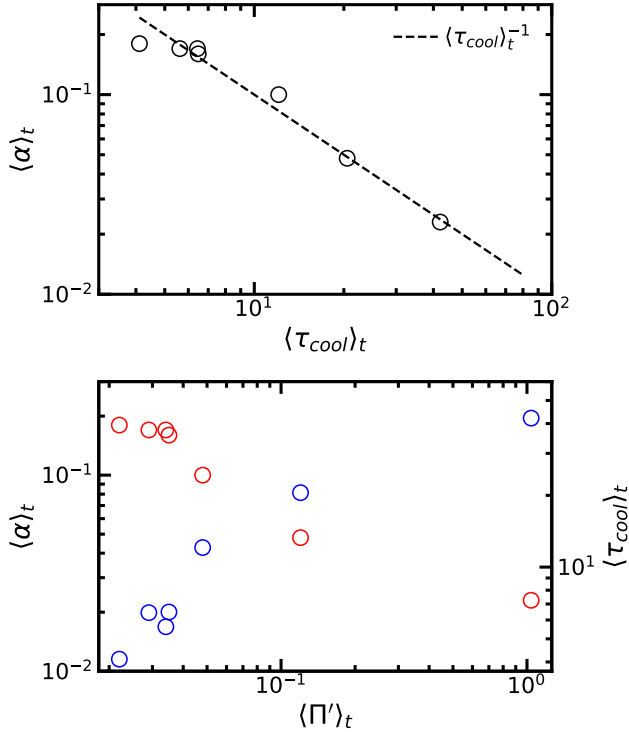


Figure 10. Averaged turbulent parameters, cooling times and pressure ratios in the gravito-turbulent states. Upper panel: $\langle \alpha \rangle_t$ plotted against $\langle \tau_{\text{cool}} \rangle_t$ to demonstrate heating-cooling equilibrium; Lower panel: $\langle \alpha \rangle_t$ (red circles) and $\langle \tau_{\text{cool}} \rangle_t$ (blue) plotted against $\langle \Pi' \rangle_t = \langle \langle P_{\text{gas}} \rangle \rangle_t / \langle \langle P_{\text{rad}} \rangle \rangle_t$ to show the effect of radiation pressure on the stability boundary.

However, the distribution of ρ and Π become quite inhomogeneous in the midplane, with low density regions where radiation pressure dominates appearing, while the bound regions cool off to become local minima of the radiation pressure fraction. Over the first cooling timescale, Q nearly monotonically decreases, but even as the disk becomes gravitationally unstable it cannot generate enough turbulence to balance cooling. Once bound fragments form, no quasi-steady state can be achieved. The overall behavior of τ_{cool} is also similar in the two cases, with an initial increase in a brief phase of steady cooling, followed by a secular decrease after turbulence develops. While the case S1e501.5e-8 has a $\tau_{\text{cool}} < 1$ upon the point of fragmentation, the case S1e501.8e-8 fragmented at $\tau_{\text{cool}} \sim 7$; this implies that $\Pi' \sim 0.1$ can already prevent the disk from maintaining a turbulence of $\alpha \sim 0.1$. Other fragmentation cases with large surface density on the $\Pi' < 1$ side show similar behavior, with larger Π' runs being able to fragment at larger τ_{cool} . Specially, the run S2e61e-7 (top-most red dot in Figure 4) undergoes collapse at $\tau_{\text{cool}} \sim 30$.

Despite the increase of critical cooling time at larger Π' as consistent with Figure 10, the outcome in fragmentation cases with non-negligible $\Pi' < 1$ are still similar to those well-studied in the gas-pressure dominated Jeans instability theory. Formation of bound regions has characteristic length scale $\sim L_T$ (Goodman & Tan 2004, see their §3.2), with *initial* masses comparable to the Jeans mass ΣL_T^2 . However, we do not follow long term development of these clumps in this paper. We therefore cannot determine if merger and accretion renders larger final masses when structures become dense enough for nuclear fusion or core-collapse, or if alternatively the initial collapsing objects fragment into lower masses. While our current simulations do not permit us to reach any conclusions regarding initial mass function for star formation in AGN disks, §5 provides some rough estimates of initial fragment masses.

We have remarked that there are also marginally non-fragmentating simulations along the stability boundary that never settle into a steady-state. In these runs, each time the disk cools down to a relatively small $Q \sim 0.5$ and 1-2 dense clumps begin to form in the midplane, strong in-homogeneous turbulence develops abruptly and heats the disk up to $Q \gtrsim 1$ again within just a few dynamical timescales. As the disk reaches a hotter state, the outburst of turbulent heating dies out along with dispersal the bound clumps, but subsequently the disk cools down again with a small background turbulence unable to fully balance radiative cooling. We typically see 2–3 of these cycles in our marginal cases before we stop the simulation, and without running for up to a thousand dynamical timescales there is no way to know whether the disk can reach a quasi-steady turbulent state. Since these models have quite distinctive behavior, however, we identify them as a third “marginally unstable” scenario (purple open circles in Figure 4), but do not discuss them in detail. If these cases can stabilize given sufficient simulation time at larger Π' than our gravito-turbulent cases, then Figure 10 should be seen as a conservative estimate of the critical α , suggesting that there is still room too support slightly larger quasi-steady turbulence against cooling.

4.5. Radiation Pressure Dominated Fragmentation Cases

Moving further left in the (Σ, Ω) parameter space (see Figure 4), there is a group of runs along the initial $\Pi = 1$ contour that fragmented with $\Pi' \gtrsim 1$ and behave similarly to those described in 4.4. To better compare with the gas pressure dominated fragmentation outcomes, we present result from fragmenting runs S3e504e-9 and S1e502e-9 with final $\Pi' \sim 30$. The former case has

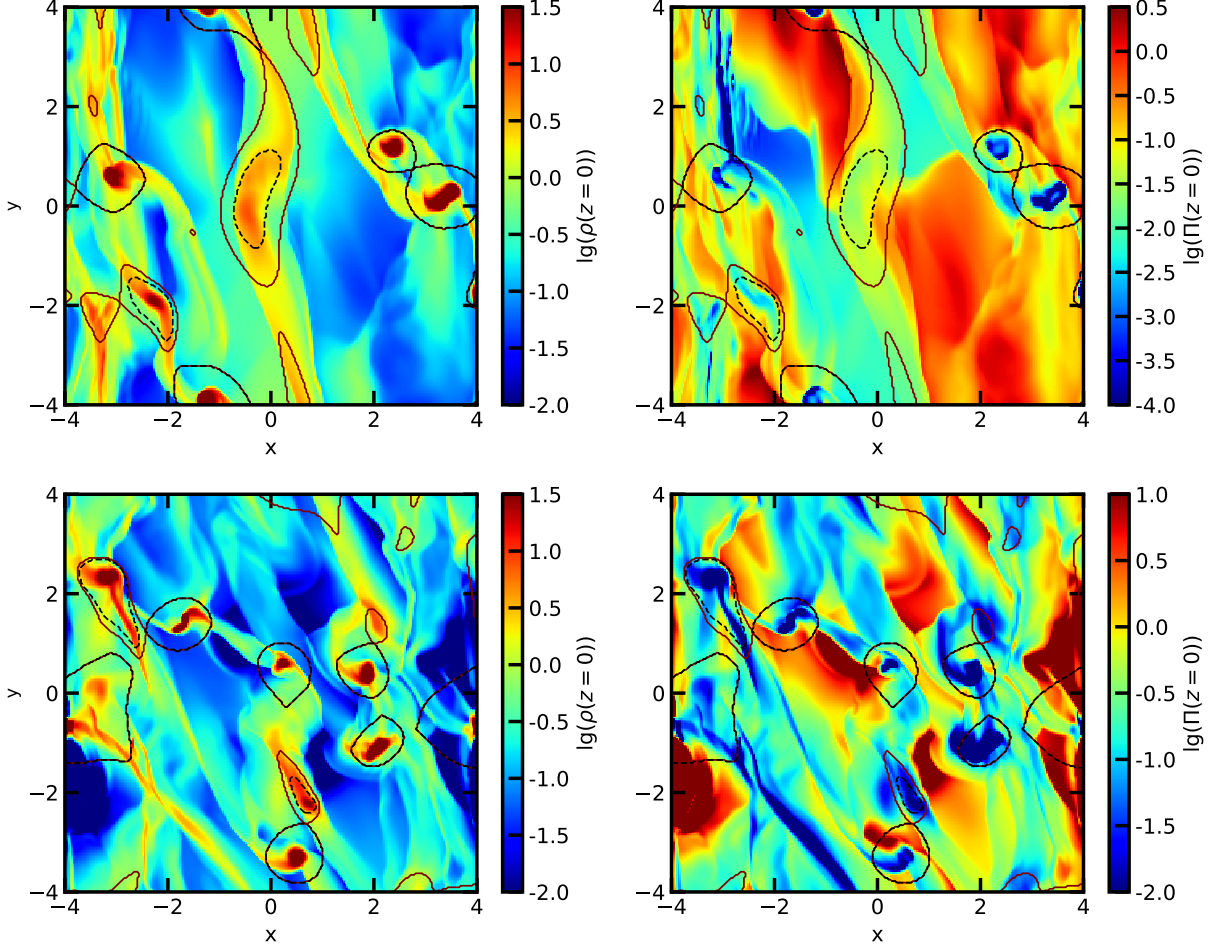


Figure 11. Snapshots of midplane density and Π for two exemplary gas-dominated fragmentation cases with final $\Pi' \lesssim 0.1$. Top panels show S1e501.8e-8, bottom panel S1e501.5e-8.

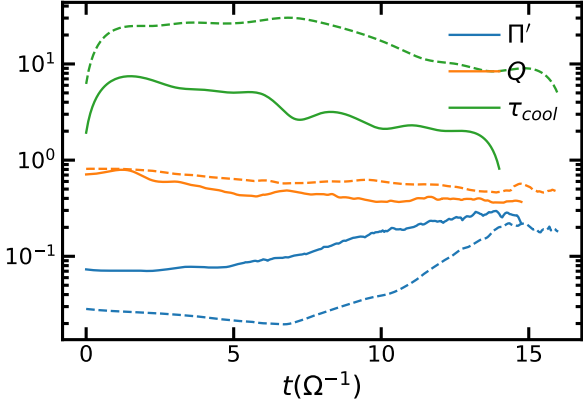


Figure 12. Evolution of average variables Π' , Q , and τ_{cool} in cases S1e501.8e-8 (dashed lines) and S1e501.5e-8 (solid lines).

$\tau_{\text{cool}} \sim 10$, but boundary values from Figure 10 suggests that in the case of $\Pi' \sim 0.1$ we already require $\tau_{\text{cool}} > 10$ to stabilize, so for much larger Π' , fragmen-

tation is expected. The latter case has a cooling time within the $\tau_{\text{cool}} \sim 3$ boundary so it would fragment even by classical standards, and we expect it to be even more susceptible to fragmentation in the radiation dominated situation.

From Figure 13 and Figure 14 (plotted in the same manner as Figure 11 and Figure 12), we observe that the decrease in Q also become irreversible up to the point of fragmentation. The result from S3e504e-9 reconfirms that in the radiation dominated regime, the classical criterion no longer applies since $\tau_{\text{cool}} \gtrsim 10$ still cannot prevent fragmentation. The initial fragment sizes are still of order L_T , meaning that the pressure within these fragments is supported by both gas and radiation.

For run S1e502e-9, a final $\tau_{\text{cool}} < 1$ is accompanied by rapid fragmentation after $\sim 5\Omega^{-1}$. A notable feature is that the width of density waves upon fragmentation, and the size of subsequent clumps (as seen in Figure 13) are distinctively smaller than in other fragmentation cases.

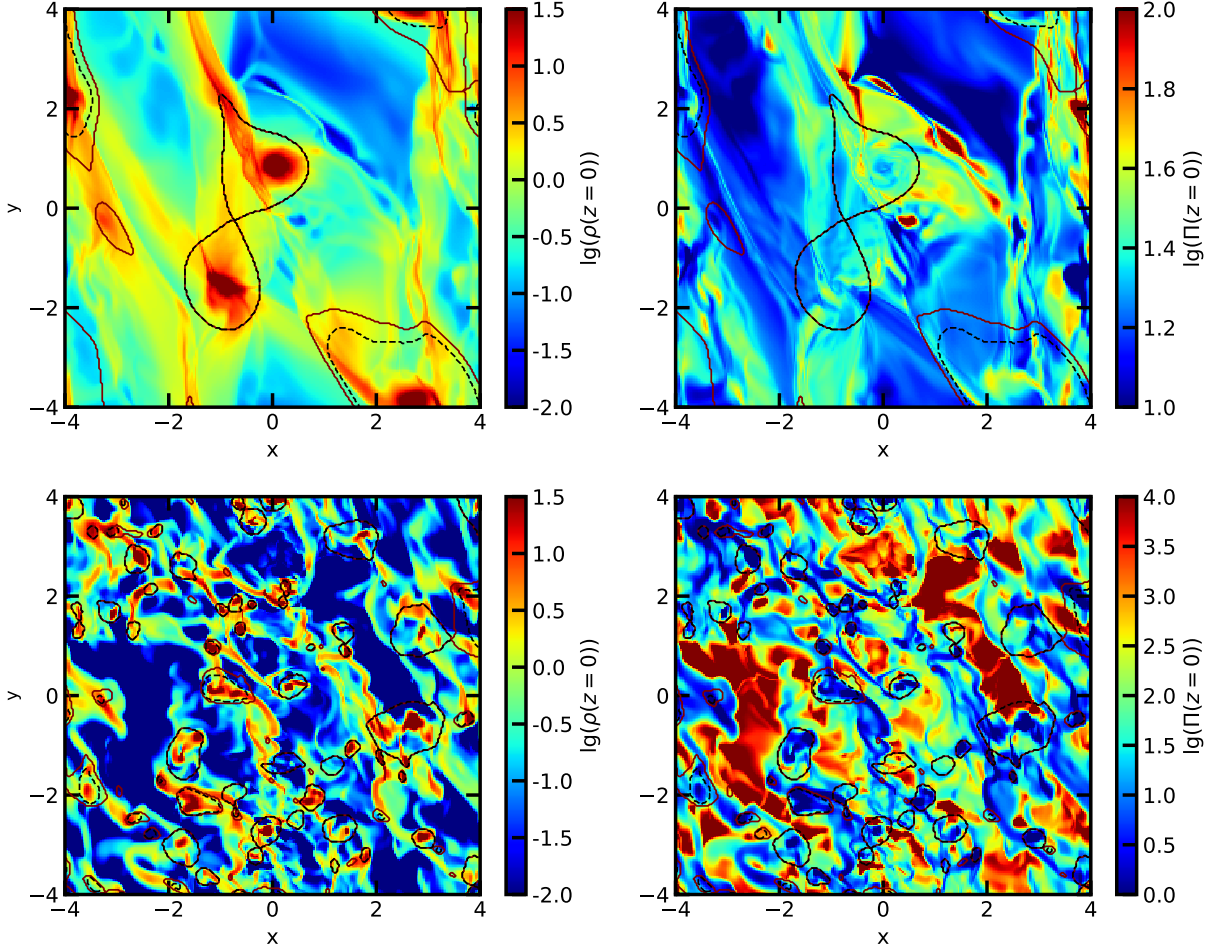


Figure 13. Midplane slices of ρ and Π for radiation-dominated fragmentation cases S3e504e-9 (top) and S1e502e-9 (bottom).

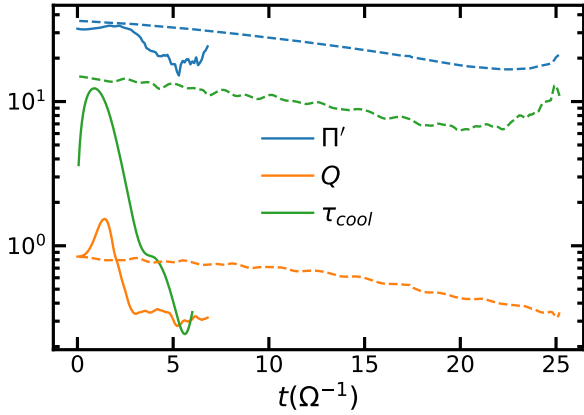


Figure 14. Evolution of average variables Π' , Q , and τ_{cool} in cases S3e504e-9 (dashed lines) and S1e502e-9 (solid lines).

In the midplane where fragments first appear, the Jeans length can be expressed as

$$L_J = c_s \left(\frac{\pi}{G\rho_0} \right)^{1/2} = \frac{c_s \Omega}{\pi G \Sigma} \left(\frac{\Omega^2}{\rho_0 \pi G} \right)^{1/2} L_T, \quad (38)$$

where the characteristic sound speed $c_s \approx Q_T \pi G \Sigma / \Omega$ and midplane density $\rho_0 \approx \Omega^2 / (2\pi G Q)$ will result in $L_J \approx Q_T \sqrt{2Q} L_T$. While we consistently observe bound regions with typical size/spacing of $L_J \lesssim L_T$ in the afore-mentioned fragmenting runs, for S1e502e-9 in the $\tau_{cool} < 1$ limit the size instead becomes more comparable to the gas-pressure Jeans length:

$$L_{J,gas} = c_{s,gas} \left(\frac{\pi}{G\rho_0} \right)^{1/2} \approx \frac{L_J}{(1 + \Pi')^{1/2}} < L_J. \quad (39)$$

Here, $c_{s,gas}$ is the sound speed from gas pressure only. The Π distribution also suggests for this particular case, radiation quickly escapes bound clumps and they are supported exclusively by gas pressure. In S3e504e-9, there are also small filaments of density fluctuations on the scale of $L_{J,gas}$, but it is still the total pressure that determines the characteristic fragment size. We performed two additional runs with higher resolution S3e504e-9_res and S1e502e-9_res (smaller horizontal box size to save computation time) in which the respective $L_{J,gas}$ at $Q \sim 1$ is properly resolved by ~ 10 grid

zones. Since we never reach a steady state and upon fragmentation Q may reach as low as ~ 0.3 , such resolution may be necessary. Nevertheless, in the high resolution runs the qualitative fragmentation outcomes have not changed and the characteristic fragment size difference is still apparent. This dichotomy may be explained by a radiation diffusion rate criterion, separate from the fragmentation/stability boundary, which we will elaborate in §4.7.

4.6. Radiation Pressure Dominated Gravitational-turbulent Case

The one exceptional radiation dominated case in Figure 4 is S2e602e-8_res, which has an initial dimensionless cooling time $\tau_{\text{cool}} \sim 100$. For this model with extremely weak radiative cooling, the simulation reaches a quasi-steady state with a large radiation pressure fraction, analogous to the previous gas pressure dominated cases S1e502e-9 and S3e504e-9. Because it is safest to resolve the gas Jeans length for such simulations, we choose a small box size of $4 \times 4 \times 2L_T^3$ with high resolution $256 \times 256 \times 128$, similar to S1e502e-9_res and S3e504e-9_res which converge with their low resolution counterparts in their fragmentation outcomes. We run this simulation for 400 orbits without runaway gravitational collapse. The computational cost for this run is about 10 Million CPU core hours.

Snapshots of the midplane ρ, T, Π distribution are shown in Figure 15. Note that the simulation domain is smaller than in Figure 5. Compared to the fiducial gas pressure dominated simulation, the turbulence level for S2e602e-8_res is very low and density/temperature fluctuations are considerably smaller. In addition to structures on the Jeans scale $\sim L_J$, there are also much smaller scale fluctuations in the x direction, possibly related to $L_{J,\text{gas}}$ as previously discussed.

To quantify the structure in S2e602e-8_res, we plot the midplane energy spectrum² in Figure 16 with solid lines. Additionally, we plot the spectrum from the fiducial simulation fiducial with dashed lines. The spectra are multiplied by a factor of $k^{5/3}$ to indicate the break wavenumbers clearly (e.g. Booth & Clarke 2019, Figure 5). We observe that in gas pressure dominated model fiducial there are spectral breaks in both x and y directions around $kL_T \sim 2\pi$, in the radiation dominated run the $U(k_x)$ spectrum does extend to $\sim kL_T/\sqrt{1 + \langle \Pi' \rangle_t} \sim 2\pi$ before breaking. We briefly discuss the origin of these modes in §4.7.

² We employ the total internal energy U for Fourier analysis because the time fluctuation in its spectrum is smaller compared to other variables.

Evolution of globally averaged variables are shown in Figure 17 (analogous to Figure 6). The run stabilizes after $\sim 100\Omega^{-1}$, converging to $\langle \tau_{\text{cool}} \rangle_t \approx 150$, $\langle \alpha \rangle_t \approx 0.006$ and $\langle \Pi' \rangle_t \approx 38$. Other measurements are provided in Table 2. The averaged vertical profiles in code units are plotted in Figure 18 in comparison to initial conditions, showing relatively extended distributions with a smaller $\langle h \rangle_t/L_T = 0.23$, similar to the case with significant radiation S2e601e-7_z shown in Figure 9. Although for all other cases in Table 2 a trend of $\langle h \rangle_t/L_T$ and $\langle Q_T \rangle_t$ increasing with $\langle \Pi' \rangle_t$ is manifested along the stability boundary, a larger $\langle Q_T \rangle_t$ is not seen in run S2e602e-8_res, which may be because S2e602e-8_res is not a boundary case. This suggests that for $\Pi' \sim 10 - 30$ there is still room to stabilize at lower τ_{cool} .

Generally, the existence of cases like S2e602e-8_res do suggest that once cooling is weak enough, we can end up on a branch of gravito-turbulent states with low turbulence, on the other side of the (Σ, Ω) parameter space. However, from Figure 10 we expect such quasi-steady states to have $\alpha \lesssim 0.02$, comparable to if not smaller than α_{MRI} , therefore the significance of such cases is limited in a realistic disk environment.

4.7. Connection to Slow and Rapid Diffusion

The general behavior of linear gravitational instability in a radiation-pressure-dominated environment has been discussed by Thompson (2008), who takes into account the destabilizing influence of radiative diffusion. Particularly relevant here is his analysis for a homogeneous, optically-thick medium in uniform rotation (his Appendix A). That analysis carries over to the shearing box if restricted to axisymmetric modes ($k_y = 0$), provided that the total wavenumber $k = \sqrt{k_x^2 + k_z^2}$ is larger than the reciprocal of the vertical density scale height (H). For axisymmetric modes, radial shear influences stability only through its effect on the epicyclic frequency; since the latter is $\kappa = 2\Omega$ for uniform rotation but $\kappa = \Omega$ in a Keplerian shearing box, we replace Ω with $\Omega/2$ in Thompson's formulae. In particular, Thompson's $Q \equiv \Omega^2/\pi G\rho$ corresponds to $Q/2$ for us.

In the radiation-pressure-dominated regime where $\Pi \gg 1$ but $Q \gtrsim 1$, it is possible to find wavenumbers $k > H^{-1}$ such that $c_{s,\text{gas}}^2 k^2 < 4\pi G\rho < c_s^2 k^2$; here $c_{s,\text{gas}}^2 = P_{\text{gas}}/\rho = c_s^2/\Pi$ is the squared sound speed based just on the thermal pressure. Under these conditions, Thompson (2008)'s fifth-order dispersion relation (A2) always has at least one unstable root. The unstable modes have $k_z \neq 0$, which undercuts the stabilizing influence of the epicyclic frequency. In other words, when

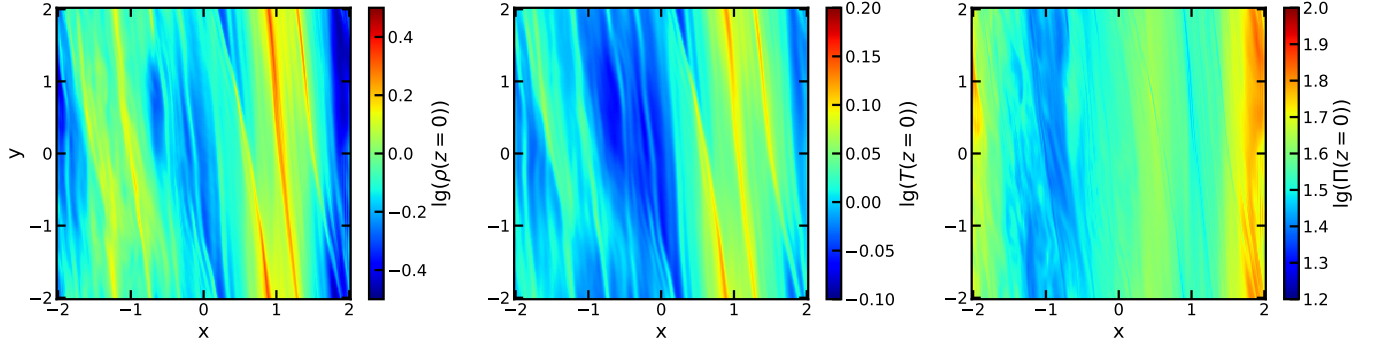


Figure 15. Slices of midplane density, temperature and radiation pressure fraction Π distribution at the final time ($t = 400\Omega^{-1}$) in radiation-dominated gravito-turbulent model `G2e602e-8_res`. The density and temperature are normalized by initial values. The length unit is $L_T = \pi^2 G \Sigma / \Omega^2$.

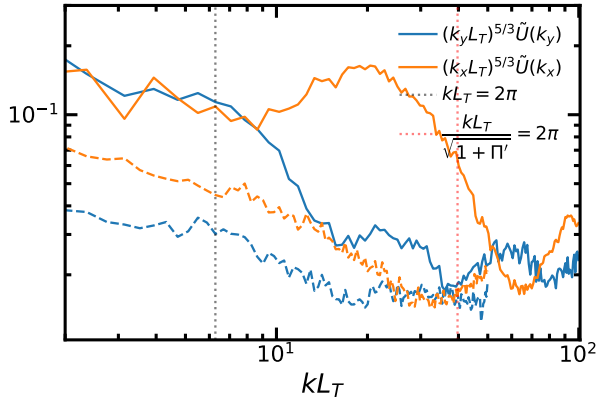


Figure 16. Power spectrum of midplane total internal energy U for gas pressure dominated gravito-turbulent case fiducial (dashed lines), versus radiation pressure dominated gravito-turbulent case `G2e602e-8_res` (solid lines), scaled with $k^{5/3}$. Blue lines and orange lines indicate spectrum in x and y directions, respectively. $\tilde{U}(k) = U(k) / \sum_k U(k)$ is the normalized spectrum density.

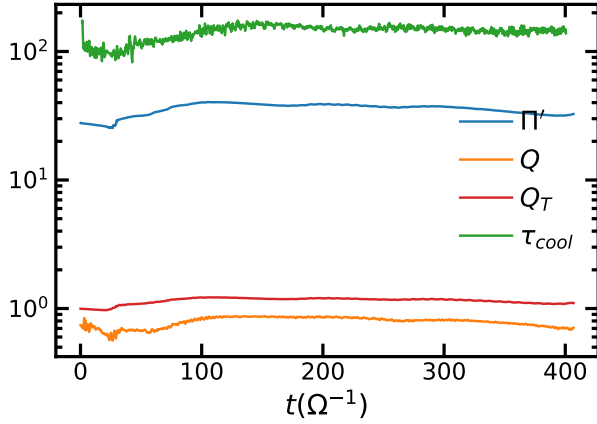


Figure 17. The evolution of globally averaged variables Q , Q_T , τ_{cool} , and Π' in the radiation dominated gravito-turbulent simulation `S2e602e-8_res`.

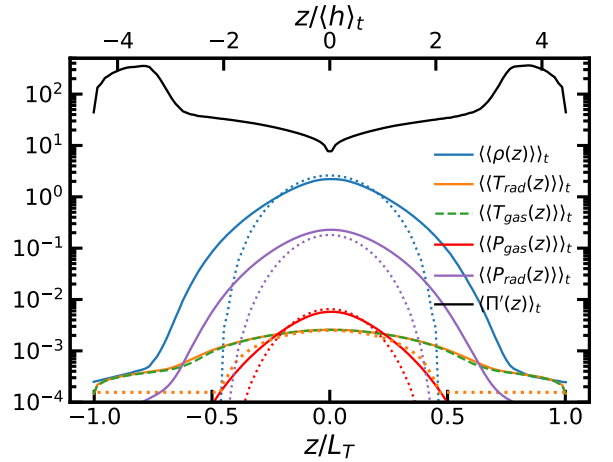


Figure 18. The horizontally and temporally averaged vertical profiles of density, gas/radiation temperature, and gas pressure in code units for the radiation-dominated run in quasi-steady state.

$P_{\text{rad}} \gg P_{\text{gas}}$, our shearing boxes are always formally axisymmetrically unstable on scales smaller than the vertical scale height but larger than the isothermal Jeans length $L_{J,\text{gas}} = 2\pi/k_{J,\text{gas}}$ for $k_{J,\text{gas}} = \sqrt{4\pi G \rho} / c_{s,\text{gas}}$.

The small-scale instability depends, however, upon radiative diffusion, so that density contrasts can grow without perturbing the radiation pressure. Thompson distinguishes regimes of slow vs. rapid growth via the dimensionless parameter

$$\chi \approx \frac{ck^2}{3\kappa\rho(4\pi G\rho)^{1/2}}, \quad (40)$$

which compares the rate of diffusion at wavenumber k to the dynamical frequency $\sqrt{4\pi G\rho}$. We shall use the notations χ_J and $\chi_{J,\text{gas}}$ for χ evaluated at the wavenumbers $k = 2\pi/L_J = \sqrt{4\pi G\rho}/c_s$ (i.e., the Jeans wavenumber based on total pressure) and $k = k_{J,\text{gas}}$ (i.e. based on thermal pressure), respectively. Under the above-mentioned conditions where the small-scale mode exists,

its growth rate is comparable to the dynamical frequency when $\chi_{J,\text{gas}} \gg 1$ (i.e. short diffusion time over the gas Jeans length), but slower by a factor $\sim \chi_{J,\text{gas}}$ in the opposite limit.

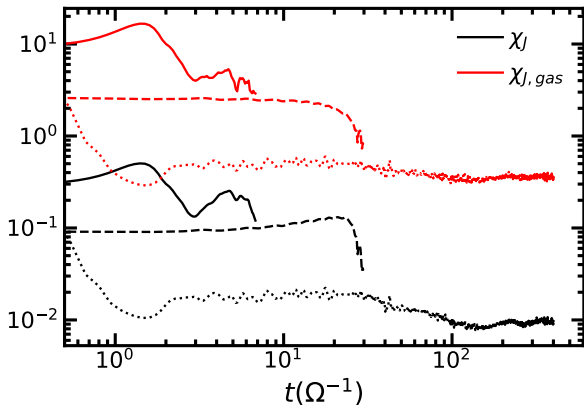


Figure 19. The diffusion parameter Equation (40) at the Jeans scale based on total pressure (black) and gas pressure only (red) for radiation-pressure-dominated runs S1e502e-9 (solid), S3e504e-9 (dashed), S2e602e-8_res (dotted).

It can be shown from Equation 10 that $\chi_J \sim \tau_{\text{cool}}^{-1}$ when $Q \sim 1$. In Figure 19 we plot the time evolution of χ_J and $\chi_{J,\text{gas}}$ from three radiation-pressure-dominated runs. Run S1e502e-9 diffuses rapidly even on the scale of the disk thickness ($\chi_J \sim 1$ at its maximum); for this model τ_{cool} plunges below unity (Figure 12), and the disk quickly fragments (Figure 11, lower row). Run S2e602e08_res illustrates the opposite extreme, where diffusion on the Jeans length defined by the gas pressure is nearly entering the slow regime ($\chi_{J,\text{gas}} \sim 1$), and $\tau_{\text{cool}} \gg 1$ as $\chi_J \ll 1$ (Figure 17). At the end of this run ($t = 400\Omega^{-1}$) one sees fine and mildly nonlinear density filaments that plausibly result from the axisymmetric small-scale instability in the regime of slow diffusion where $\chi_{J,\text{gas}} < 1$ (Figure 15). It is possible that this case might eventually fragment if it were continued to longer times.

If non-fragmentation is associated with a slow diffusion even on the gas Jeans scale ($\chi_{J,\text{gas}} \lesssim 1$), this requirement roughly translates to $\tau_{\text{cool}} \gtrsim \Pi$, equivalent to having the cooling time of *gas* thermal energy (instead of gas+radiation energy) longer than the dynamical timescale, in the radiation pressure dominated regime.

Purely from the numerical simulations, we do not currently have sufficient data to verify whether the critical cooling time in the radiation dominated regime does converge to some power law in Π' in the limit of large Π' . In particular, we note that the exemplary simulation

S2e602e-8_res is *not* a marginally stable case, and lower τ_{cool} may still be allowed. However, we re-emphasize that as far as physical situations are concerned, we expect the critical cooling time to be at least $\gtrsim 50$ for radiation-dominated ($\Pi' > 1$) gravito-turbulence (Figure 10), where in an AGN accretion disk context MRI can already provide sufficient heating to suppress gravitational instability.

It is also possible that the small-scale modes might be entirely suppressed by the introduction of additional physics. In particular, support provided by a magnetic field, unlike that provided by thermal pressure, would not be undercut by radiative diffusion, and the attendant magnetorotational turbulence might disrupt filaments even if they formed.

However, non-self-gravitating simulations by Turner et al. (2003, and references therein) have shown that the combination of MRI and radiation pressure can *enhance* density contrasts, provided that the radiation is able to diffuse across an MRI wavelength on timescales $\sim \Omega^{-1}$, leaving only the gas pressure to resist compression by the turbulent magnetic field. Simulations of galactic disks also show that with moderate-strength magnetic fields (but without radiation), MRI enhances gravitational instability because it undermines stabilization by Coriolis forces (Kim et al. 2002, 2003). Other recent studies in the protoplanetary disk context suggest that MRI induces additional small-scale modes in gravito-turbulent disc regions which could lead to formation of fragments significantly smaller than in GI-only simulations (Deng et al. 2020, 2021). Simulations with self-gravity, radiation, *and* magnetic field will probably be needed to explore the interaction between all these effects that are potentially relevant to AGN accretion disks.

5. DISCUSSION

5.1. Implication for Accretion Disk Structure

In our gas pressure dominated simulations, we confirm the maximum turbulent stress that quasi-steady gravito-turbulence can support is $\alpha \sim 0.2$, against a cooling timescale of $\tau_{\text{cool}} \sim 3 - 5$. This suggests that in the low \dot{M} , $\Pi \ll 1$ regime, a quiescent $Q_T \sim 1$ AGN accretion disk heated by gravito-turbulence can extend from the self-gravitating radius r_{sg} of the inner MRI-heated standard disk, towards an outer boundary where the radiative cooling timescale drops to $\tau_{\text{cool}} \sim 4\Omega^{-1}$, beyond which fragmentation and star formation dominates.

At high accretion rates, however, the self-gravitating region of an AGN accretion disk is radiation dominated. For a standard disk with turbulent parameter α_{MRI} heated by MRI, the outer boundary r_{sg} where Q_T drops below 1 can be expressed in terms of the accretion rate

\dot{M} and α_{MRI} . This $r_{\text{sg}}(\dot{M})$ relation should coincide with the mapping between contours of \dot{M} and their *intersection* with the $\tau_{\text{cool}} \sim \alpha_{\text{MRI}}^{-1} \sim 50$ contour in our $Q_T = 1$ plane e.g. [Figure 3](#), which shows that Π at the intersection $r_{\text{sg}}(\dot{M})$ always increases with \dot{M} , and $\Pi(r_{\text{sg}}) \gtrsim 1$ when $\dot{M} \gtrsim \dot{M}_{\odot}/\text{yr}$.

More quantitatively, the radiation fraction Π at r_{sg} satisfies ([Goodman & Tan 2004](#), modified from their Equation 18)

$$[1 + \Pi(r_{\text{sg}})]^{-1/4} \Pi(r_{\text{sg}})^{-3/4} = 0.416 \left(\frac{\alpha_{\text{MRI}}}{0.02} \right)^{1/3} \times \left(\frac{\kappa}{0.4 \text{cm}^2/\text{g}} \right)^{-1/2} \left(\frac{\mu}{0.6 m_p} \right)^{-1} \left(\frac{\dot{M}}{2.2 \dot{M}_{\odot}/\text{yr}} \right)^{-1} \quad (41)$$

which is consistent with the critical accretion rate from our setup.

As the steady-state Π increases in our suite of gravito-turbulent simulations along the fragmentation boundary (see [Table 2](#), [Figure 4](#) and [Figure 10](#)), due to the increasing destabilizing influence of radiation pressure, τ_{cool} continues to increase while α decreases, until for $\Pi \gtrsim 1$, the minimum τ_{cool} reaches ~ 50 . This suggests that Eddington (for $M_{\text{SMBH}} \lesssim 10^8 M_{\odot}$) or near-Eddington (for $M_{\text{SMBH}} \sim 10^9 M_{\odot}$) radiation dominated AGN accretion disks simply cannot have a quasi-steady gravito-turbulent region beyond r_{sg} , since gravito-turbulence could not provide significantly larger heating compared to MRI. This suggests that the disk directly switches to a star-forming region without a transition zone that has quasi-steady gravitationally driven turbulence and accretion.

In principle, the energy requirements to maintain thermal equilibrium in the star-forming region can be maintained by star formation feedback, similar to the overall situation in star-forming galactic disks ([Ostriker et al. 2010](#); [Ostriker & Shetty 2011](#); [Ostriker & Kim 2022](#)), and this need not require $Q_T \sim 1$ since turbulent dissipation and rapid cooling allow collapse to occur at scales $\lesssim H$. To continue feeding gas to the inner disk, α is maintained to be some maximum value that is ~ 0.3 for $\Pi \ll 1$, or smaller than $\lesssim 0.02$ for radiation pressure dominated disks, although decoupled from the energy equation. Alternatively, the accretion radial velocity may be parameterized by $\dot{M}/2\pi r \Sigma = v_r = mh\Omega r$ instead of $\sim \alpha h^2 \Omega r$, if accretion is mainly driven by global instabilities ([Thompson et al. 2005](#)) or large-scale magnetic torques ([Sanghyuk Moon et al 2023](#), ApJ submitted).

5.2. Implication for Stellar Evolution in AGN Disks

In most fragmenting cases, the fragments' *initial* masses are of order the Jeans mass,

$$M_J = \Sigma L_J^2 \approx \Sigma \left(\frac{\pi^2 G \Sigma}{\Omega^2} \right)^2 \approx 20 M_{\odot} \Sigma_{-5}^3 \Omega_{-8}^{-4}, \quad (42)$$

as predicted by classical theories and as found in numerical simulations of gravitationally-unstable disks (e.g. [Kim et al. 2002, 2003](#)) For $t_{\text{cool}} \ll \Omega^{-1}$, in the radiation pressure dominated case (see [§4.5](#)), we find that radiative diffusion can be very fast and the fragments instead have masses of

$$M_{J,\text{gas}} = \Sigma \frac{L_J^2}{\Pi} \approx \Sigma \left(\frac{\pi^2 G \Sigma}{\Omega^2} \right)^2 \frac{1}{\Pi} \approx 2000 M_{\odot} \Sigma_{-5}^{1.5} \Omega_{-9}^{-2}. \quad (43)$$

Since in the radiation pressure dominated regime $\Pi \propto \Sigma^{1.5} \Omega^{-2}$ ([Equation 6](#)), the initial masses can still be very large for super Eddington AGN disks with high radiation pressure fraction. Nevertheless, the initial masses of these fragments may not be directly relevant to their final masses, since through either collisions or gas accretion they may quickly grow towards a mass limit constrained by Hill radius isolation ([Goodman & Tan 2004](#)) or Eddington limit ([Cantiello et al. 2021](#); [Jermyn et al. 2022](#)).

Generally, our simulation outcomes strongly favor star formation in radiation pressure dominated AGN disks. The rapid accretion and pollution of disk gas by the massive stars that are formed here, and possibly their eventual supernovae, may contribute to super-solar metallicity abundances in AGNs ([Hamann & Ferland 1999](#); [Hamann et al. 2002](#)). The long-term evolution of massive stars may leave behind embedded stellar mass black holes (EBHs) that could provide extra heating through accretion feedbacks ([Gilbaum & Stone 2022](#)), and also relevant to production of gravitational waves (GW) that may contribute to LIGO-Virgo events ([McKernan et al. 2012, 2014](#); [Stone et al. 2017](#); [Tagawa et al. 2020](#); [Samsing et al. 2022](#); [Li et al. 2022](#)). In particular, BBH mergers in an AGN disk may produce electromagnetic counterpart that could differentiate them from other merger channels ([Graham et al. 2020](#)).

5.3. Future Prospects

Given adequate computational resources, it will be possible to perform a more extensive parameter survey over (Σ, Ω) space, in order to map out a more complete $\Pi - \tau_{\text{cool}}$ scaling that extends far into the radiation dominated regime on [Figure 4](#). Nevertheless, with MRI present as an auxiliary heating source, our finding of a $\tau_{\text{cool}} \gtrsim 50$ constraint up to $\Pi \sim 1$ is sufficient evidence to declare our major conclusion: super Eddington accretion disks will always fragment beyond r_{sg} , and

$\tau_{\text{cool}} \gtrsim 50, \alpha < \alpha_{\text{MRI}}$ gravito-turbulent states for even larger Π are possible (e.g. §4.6) but not physically significant except in situations where MRI is suppressed.

A more meaningful direction for further study may be to extend the currently explored parameter space to a more realistic setup. In this paper, we have assumed constant frequency-averaged opacity κ and a gray model $\kappa_R = \kappa_P$ for convenience in estimating initial cooling times and comparing with analytical disk profiles. It would be straightforward to instead implement realistic opacities as functions of density and temperature in subsequent studies.

A caveat of our study is that we only focus on sketching the fragmentation boundary and do not follow the evolution of the gravitationally bound structures that form. Since we expect star formation to generically develop in the outer regions of AGN disks (shortly beyond r_{sg} for near-Eddington, radiation dominated cases), it will be very interesting to follow this in more detail. In general, sink particles are needed to avoid numerical singularities from gravitational collapse, and these can be coupled to treatments of radiation feedback, stellar winds, and supernovae given assumptions of the stellar population that is produced (e.g. Gong & Ostriker 2013; Skinner & Ostriker 2015; Kim & Ostriker 2017; Kim et al. 2017; Lancaster et al. 2021). With the addi-

tion of adaptive mesh refinement to follow small-scale fragmentation, it will be possible to follow the long-term evolution of the initial Jeans-scale clumps that are the dominant type of outcome in our $\Pi \gtrsim 1$ models. Such simulations, either local or global, can inform us both regarding the mass spectrum of stars formed, and whether energy equilibrium with star formation heating is indeed maintained, either in a state of marginal large-scale gravitational instability (Thompson et al. 2005), or a state of vertical thermal and dynamical equilibrium more similar to nuclear rings fed by bars at larger scale (Moon et al. 2021).

ACKNOWLEDGMENTS

YXC thanks Wenrui Xu, Chang-Goo Kim, Alwin Mao, Douglas Lin, Eliot Quataert, Xue-Ning Bai, Jane Dai, Kaitlin Kratter, Minghao Guo for helpful discussions. We also acknowledge computational resources provided by the high-performance computer center at Princeton University, which is jointly supported by the Princeton Institute for Computational Science and Engineering (PICSciE) and the Princeton University Office of Information Technology. The work of ECO is supported by grant 510940 from the Simons Foundation. The Center for Computational Astrophysics at the Flatiron Institute is supported by the Simons Foundation.

APPENDIX

A. INITIAL EQUILIBRIUM PROFILE

To set up a fiducial initial profile, we assume $\Pi := P_{\text{rad}}/P_{\text{gas}}$ is constant in the bulk of the disk, which suggests a $P(z) = K\rho^{4/3}(z)$ polytropic profile that is analytically solvable given fixed parameters Σ, Ω , and an additional Q (or equivalently the midplane density ρ_0 , see eq. (20)) that controls the onset of GI³. Although Q is not conserved throughout the simulation, we expect $Q \sim Q_T \sim 1$ if our initial conditions indeed evolve into steady states, consistent with the arguments in §2.

We can express the constant K in terms of ρ_0 and Σ (Jiang & Goodman 2011, using Equations A2, A5):

$$\mathcal{H} := \frac{\Sigma}{4\sqrt{2}\rho_0 I_3(Q)} = \sqrt{\frac{K}{\rho_0^{2/3}\pi G}} \quad (\text{A1})$$

Where \mathcal{H} is a normalization vertical length and a proxy for the photosphere height. Here we define $I_k(Q)$ as

$$I_k(Q) \equiv \int_0^1 \frac{(1-w^2)^k dw}{\sqrt{2Q+1 + \sum_{i=1,2,3} (1-w^2)^i}}. \quad (\text{A2})$$

Approximations accurate to % 1 are (Jiang & Goodman 2011, Equation 8):

$$I_3(Q) \approx \frac{0.323}{\sqrt{Q+1.72}}, \quad I_4(Q) \approx \frac{0.287}{\sqrt{Q+1.72}}, \quad (\text{A3})$$

³ the polytropic assumption is used only for this initialization; the subsequent evolution obeys the full energy equation

Given \mathcal{H} determined by Q, ρ_0, Σ , the vertical distribution of density $\rho(z)$ is initialized according to

$$\frac{z}{\mathcal{H}} = \int_0^{\sqrt{1-\theta}} \frac{2\sqrt{2}dw}{\sqrt{2Q+1 + \sum_{i=1,2,3} (1-w^2)^i}}, \quad (\text{A4})$$

$$\theta = [\rho(z)/\rho_0]^{1/3}$$

It can be shown that $\rho(z)$ converges to the following analytic relation when Q approaches infinity (non-self-gravitating case):

$$[\rho(z)/\rho_0]^{1/3} = \left(1 - \frac{z^2\Omega^2}{8K\rho_0^{1/3}}\right). \quad (\text{A5})$$

The specific vertical profile with constant $K = P/\rho^{4/3}$ gives coefficients for the midplane EoS $P_0(\rho_0, T_0)$ (Equation 2) as

$$\frac{\rho_0}{\rho_*} = f_\rho = \frac{1}{2Q}, \quad \frac{P_0}{P_*} = f_p = \frac{1}{32[I_3(Q)]^2} \quad (\text{A6})$$

For vertically integrated pressure P_{2D} and internal energy density U_{2D} , Equations 5 & 9 of Jiang & Goodman (2011) translate to

$$\frac{P_{2D}}{P_*l_*} = \frac{QI_4(Q)}{16[I_3(Q)]^3}, \quad U_{2D} = \left[1 - \frac{1}{2(\Pi+1)}\right] P_{2D}, \quad (\text{A7})$$

which gives us another order-unity coefficient

$$\frac{U_{2D}}{P_*l_*} = f_U = \left[1 - \frac{1}{2(\Pi+1)}\right] \frac{QI_4(Q)}{16[I_3(Q)]^3} \quad (\text{A8})$$

Apart from hydrodynamical variables, we also attempt to set up initial vertical radiation flux self-consistently. Since Π is independent of z , from the expression for optically thick radiation pressure gradient

$$\frac{dP_{\text{rad}}}{dz} = \Pi \frac{dP_{\text{gas}}}{dz} = -\kappa\rho F_z/c \quad (\text{A9})$$

Where

$$\frac{dP_{\text{rad}}}{dz} + \frac{dP_{\text{gas}}}{dz} = -\Omega^2 z - 4\pi G \int_0^z \rho(z') dz' \quad (\text{A10})$$

We can calculate the initial F_z distribution with the opacity $\kappa = \kappa_s + \kappa_R$. As one go to higher $|z|$, ρ , T as well as E_{rad} start to abruptly drop at $\sim \pm\mathcal{H}$, which is also where the cumulative optical depth falls to unity, so we fix the value of both E_{rad} and F_z outside this ‘‘photosphere’’ around $\sim \pm\mathcal{H}$ where $|F_{z,\text{max}}|/c = E_{\text{rad}} = aT_{\text{eff}}^4$ are all constants. This means regions outside photosphere does not have fixed Π anymore and is subject to optically thin cooling. Nevertheless, energy distribution outside the photosphere has little relevance to the turbulence process since gas is tenuous there. We find that as long as $|F_z|/c \lesssim E_{\text{rad}}$ beyond \mathcal{H} , the radiation profile outside the photosphere relaxes to a constant $F_{z,\text{max}} := aT_{\text{eff}}^4$ after a small timestep, which is close to the analytical prediction given in Equation 7. With the numerical solution for $F_{z,\text{max}}$, we can plot out scalings for the expected cooling timescales and local accretion rates (Figure 2 and Figure 3).

REFERENCES

- Balbus, S. A., & Hawley, J. F. 1991, ApJ, 376, 214, doi: [10.1086/170270](https://doi.org/10.1086/170270)
- Beckwith, K., Armitage, P. J., & Simon, J. B. 2011, Monthly Notices of the Royal Astronomical Society, 416, 361
- Booth, R. A., & Clarke, C. J. 2019, MNRAS, 483, 3718, doi: [10.1093/mnras/sty3340](https://doi.org/10.1093/mnras/sty3340)
- Cantiello, M., Jermyn, A. S., & Lin, D. N. C. 2021, ApJ, 910, 94, doi: [10.3847/1538-4357/abdf4f](https://doi.org/10.3847/1538-4357/abdf4f)

- Deng, H., Mayer, L., & Helled, R. 2021, *Nature Astronomy*, 5, 440, doi: [10.1038/s41550-020-01297-6](https://doi.org/10.1038/s41550-020-01297-6)
- Deng, H., Mayer, L., & Latter, H. 2020, *ApJ*, 891, 154, doi: [10.3847/1538-4357/ab77b2](https://doi.org/10.3847/1538-4357/ab77b2)
- Gammie, C. F. 2001, *ApJ*, 553, 174, doi: [10.1086/320631](https://doi.org/10.1086/320631)
- Gilbaum, S., & Stone, N. C. 2022, *ApJ*, 928, 191, doi: [10.3847/1538-4357/ac4ded](https://doi.org/10.3847/1538-4357/ac4ded)
- Goldberg, J. A., Jiang, Y.-F., & Bildsten, L. 2021, arXiv e-prints, arXiv:2110.03261. <https://arxiv.org/abs/2110.03261>
- Gong, H., & Ostriker, E. C. 2011, *ApJ*, 729, 120, doi: [10.1088/0004-637X/729/2/120](https://doi.org/10.1088/0004-637X/729/2/120)
- . 2013, *ApJS*, 204, 8, doi: [10.1088/0067-0049/204/1/8](https://doi.org/10.1088/0067-0049/204/1/8)
- Goodman, J. 2003, *MNRAS*, 339, 937, doi: [10.1046/j.1365-8711.2003.06241.x](https://doi.org/10.1046/j.1365-8711.2003.06241.x)
- Goodman, J., & Tan, J. C. 2004, *ApJ*, 608, 108, doi: [10.1086/386360](https://doi.org/10.1086/386360)
- Graham, M. J., Ford, K. E. S., McKernan, B., et al. 2020, *PhRvL*, 124, 251102, doi: [10.1103/PhysRevLett.124.251102](https://doi.org/10.1103/PhysRevLett.124.251102)
- Hamann, F., & Ferland, G. 1999, *ARA&A*, 37, 487, doi: [10.1146/annurev.astro.37.1.487](https://doi.org/10.1146/annurev.astro.37.1.487)
- Hamann, F., Korista, K. T., Ferland, G. J., Warner, C., & Baldwin, J. 2002, *ApJ*, 564, 592, doi: [10.1086/324289](https://doi.org/10.1086/324289)
- Hirose, S., & Shi, J.-M. 2017, *MNRAS*, 469, 561, doi: [10.1093/mnras/stx824](https://doi.org/10.1093/mnras/stx824)
- . 2019, *MNRAS*, 485, 266, doi: [10.1093/mnras/stz163](https://doi.org/10.1093/mnras/stz163)
- Jermyn, A. S., Dittmann, A. J., McKernan, B., Ford, K. E. S., & Cantiello, M. 2022, *ApJ*, 929, 133, doi: [10.3847/1538-4357/ac5d40](https://doi.org/10.3847/1538-4357/ac5d40)
- Jiang, Y.-F. 2021, *ApJS*, 253, 49, doi: [10.3847/1538-4365/abe303](https://doi.org/10.3847/1538-4365/abe303)
- Jiang, Y.-F., & Blaes, O. 2020, *ApJ*, 900, 25, doi: [10.3847/1538-4357/aba4b7](https://doi.org/10.3847/1538-4357/aba4b7)
- Jiang, Y.-F., & Goodman, J. 2011, *ApJ*, 730, 45, doi: [10.1088/0004-637X/730/1/45](https://doi.org/10.1088/0004-637X/730/1/45)
- Jiang, Y.-F., Stone, J. M., & Davis, S. W. 2014, *ApJS*, 213, 7, doi: [10.1088/0067-0049/213/1/7](https://doi.org/10.1088/0067-0049/213/1/7)
- Johnson, B. M., & Gammie, C. F. 2003, *ApJ*, 597, 131, doi: [10.1086/378392](https://doi.org/10.1086/378392)
- Kim, C.-G., Kim, W.-T., & Ostriker, E. C. 2011, *ApJ*, 743, 25, doi: [10.1088/0004-637X/743/1/25](https://doi.org/10.1088/0004-637X/743/1/25)
- Kim, C.-G., & Ostriker, E. C. 2017, *ApJ*, 846, 133, doi: [10.3847/1538-4357/aa8599](https://doi.org/10.3847/1538-4357/aa8599)
- Kim, J.-G., Kim, W.-T., Ostriker, E. C., & Skinner, M. A. 2017, *ApJ*, 851, 93, doi: [10.3847/1538-4357/aa9b80](https://doi.org/10.3847/1538-4357/aa9b80)
- Kim, W.-T., Ostriker, E. C., & Stone, J. M. 2002, *ApJ*, 581, 1080, doi: [10.1086/344367](https://doi.org/10.1086/344367)
- . 2003, *ApJ*, 599, 1157, doi: [10.1086/379367](https://doi.org/10.1086/379367)
- Kormendy, J., & Ho, L. C. 2013, *ARA&A*, 51, 511, doi: [10.1146/annurev-astro-082708-101811](https://doi.org/10.1146/annurev-astro-082708-101811)
- Koyama, H., & Ostriker, E. C. 2009, *ApJ*, 693, 1316, doi: [10.1088/0004-637X/693/2/1316](https://doi.org/10.1088/0004-637X/693/2/1316)
- Lancaster, L., Ostriker, E. C., Kim, J.-G., & Kim, C.-G. 2021, *ApJ*, 914, 90, doi: [10.3847/1538-4357/abf8ac](https://doi.org/10.3847/1538-4357/abf8ac)
- Levin, Y. 2007, *MNRAS*, 374, 515, doi: [10.1111/j.1365-2966.2006.11155.x](https://doi.org/10.1111/j.1365-2966.2006.11155.x)
- Li, Y.-P., Chen, Y.-X., Lin, D. N. C., & Wang, Z. 2022, *ApJL*, 928, L1, doi: [10.3847/2041-8213/ac5b61](https://doi.org/10.3847/2041-8213/ac5b61)
- Lynden-Bell, D. 1969, *Nature*, 223, 690, doi: [10.1038/223690a0](https://doi.org/10.1038/223690a0)
- Mao, S. A., Ostriker, E. C., & Kim, C.-G. 2020, *ApJ*, 898, 52, doi: [10.3847/1538-4357/ab989c](https://doi.org/10.3847/1538-4357/ab989c)
- McKernan, B., Ford, K. E. S., Kocsis, B., Lyra, W., & Winter, L. M. 2014, *MNRAS*, 441, 900, doi: [10.1093/mnras/stu553](https://doi.org/10.1093/mnras/stu553)
- McKernan, B., Ford, K. E. S., Lyra, W., & Perets, H. B. 2012, *MNRAS*, 425, 460, doi: [10.1111/j.1365-2966.2012.21486.x](https://doi.org/10.1111/j.1365-2966.2012.21486.x)
- Mihalas, D., & Mihalas, B. W. 1984, *Foundations of radiation hydrodynamics*
- Moon, S., Kim, W.-T., Kim, C.-G., & Ostriker, E. C. 2021, *ApJ*, 914, 9, doi: [10.3847/1538-4357/abfa93](https://doi.org/10.3847/1538-4357/abfa93)
- Ostriker, E. C., & Kim, C.-G. 2022, *ApJ*, 936, 137, doi: [10.3847/1538-4357/ac7de2](https://doi.org/10.3847/1538-4357/ac7de2)
- Ostriker, E. C., McKee, C. F., & Leroy, A. K. 2010, *ApJ*, 721, 975, doi: [10.1088/0004-637X/721/2/975](https://doi.org/10.1088/0004-637X/721/2/975)
- Ostriker, E. C., & Shetty, R. 2011, *ApJ*, 731, 41, doi: [10.1088/0004-637X/731/1/41](https://doi.org/10.1088/0004-637X/731/1/41)
- Paardekooper, S.-J. 2012, *MNRAS*, 421, 3286, doi: [10.1111/j.1365-2966.2012.20553.x](https://doi.org/10.1111/j.1365-2966.2012.20553.x)
- Pringle, J. E. 1981, *ARA&A*, 19, 137, doi: [10.1146/annurev.aa.19.090181.001033](https://doi.org/10.1146/annurev.aa.19.090181.001033)
- Rice, W. K. M., Armitage, P. J., Bate, M. R., & Bonnell, I. A. 2003, *MNRAS*, 339, 1025, doi: [10.1046/j.1365-8711.2003.06253.x](https://doi.org/10.1046/j.1365-8711.2003.06253.x)
- Rice, W. K. M., Lodato, G., & Armitage, P. J. 2005, *MNRAS*, 364, L56, doi: [10.1111/j.1745-3933.2005.00105.x](https://doi.org/10.1111/j.1745-3933.2005.00105.x)
- Riols, A., Latter, H., & Paardekooper, S. J. 2017, *MNRAS*, 471, 317, doi: [10.1093/mnras/stx1548](https://doi.org/10.1093/mnras/stx1548)
- Samsing, J., Bartos, I., D’Orazio, D. J., et al. 2022, *Nature*, 603, 237, doi: [10.1038/s41586-021-04333-1](https://doi.org/10.1038/s41586-021-04333-1)
- Shakura, N. I., & Sunyaev, R. A. 1973, *A&A*, 500, 33
- Shi, J.-M., & Chiang, E. 2014, *ApJ*, 789, 34, doi: [10.1088/0004-637X/789/1/34](https://doi.org/10.1088/0004-637X/789/1/34)
- Simon, J. B., Beckwith, K., & Armitage, P. J. 2012, *Monthly Notices of the Royal Astronomical Society*, 422, 2685

- Sirko, E., & Goodman, J. 2003, MNRAS, 341, 501,
doi: [10.1046/j.1365-8711.2003.06431.x](https://doi.org/10.1046/j.1365-8711.2003.06431.x)
- Skinner, M. A., & Ostriker, E. C. 2015, ApJ, 809, 187,
doi: [10.1088/0004-637X/809/2/187](https://doi.org/10.1088/0004-637X/809/2/187)
- Stone, J. M., Tomida, K., White, C. J., & Felker, K. G.
2020, ApJS, 249, 4, doi: [10.3847/1538-4365/ab929b](https://doi.org/10.3847/1538-4365/ab929b)
- Stone, N. C., Metzger, B. D., & Haiman, Z. 2017, MNRAS,
464, 946, doi: [10.1093/mnras/stw2260](https://doi.org/10.1093/mnras/stw2260)
- Tagawa, H., Haiman, Z., & Kocsis, B. 2020, ApJ, 898, 25,
doi: [10.3847/1538-4357/ab9b8c](https://doi.org/10.3847/1538-4357/ab9b8c)
- Thompson, T. A. 2008, ApJ, 684, 212, doi: [10.1086/589227](https://doi.org/10.1086/589227)
- Thompson, T. A., Quataert, E., & Murray, N. 2005, ApJ,
630, 167, doi: [10.1086/431923](https://doi.org/10.1086/431923)
- Toomre, A. 1964, ApJ, 139, 1217, doi: [10.1086/147861](https://doi.org/10.1086/147861)
- Turner, N. J., Stone, J. M., Krolik, J. H., & Sano, T. 2003,
ApJ, 593, 992, doi: [10.1086/376615](https://doi.org/10.1086/376615)